The *Magnaporthe oryzae* MAX effector AVR-Pia binds a novel group of rice HMA domain-containing proteins

Josephine H.R. Maidment[1,2]*, Svenja C. Saile[1]*, Aurélien Bocquet[2], Céline Thivolle[1], Léo Bourcet[2], Lisa-Fatimatou Planel[1], Muriel Gelin[2], Thomas Kroj[1], André Padilla[2], Karine de Guillen[2]**, Stella Cesari[1]**

[1] PHIM Plant Health Institute, Université de Montpellier, INRAE, CIRAD, Institut Agro, IRD, Montpellier, France.
[2] Centre de Biologie Structurale, INSERM, CNRS, Université de Montpellier, 29 rue de Navacelles, 34090, Montpellier, France

*Contributed equally
**Corresponding authors

Stella Cesari
Tel: +33 4 99 62 48 62
Email: stella.cesari@inrae.fr

Karine de Guillen
Tel: +33 4 67 41 77 08
Email: karine.deguillen@cbs.cnrs.fr

ORCID
Josephine H.R. Maidment: 0000-0002-8229-2718
Svenja C. Saile: 0000-0003-2258-3166
Aurélien Bocquet: 0009-0007-0082-6098
Céline Thivolle: 0009-0000-5048-3619
Léo Bourcet: 0009-0004-4568-3543
Lisa-Fatimatou Planel: 0009-0007-5159-7109
Muriel Gelin 0000-0003-1320-8663
Thomas Kroj: 0000-0002-3752-1788
André Padilla: 0000-0001-9702-4612
Karine de Guillen: 0000-0002-5037-2115
Stella Cesari: 0000-0001-8558-0371

Keywords: pathogen effector, host virulence targets, rice blast fungus, rice, protein structure, plant defence, heavy metal associated domain, MAX effector

Abstract

Phytopathogenic fungi secrete effector proteins to promote virulence. MAX (*Magnaporthe* Avrs and ToxB-like) effectors form a sequence-diverse family sharing a conserved protein structure. AVR-Pia, a MAX effector from the rice blast fungus *Magnaporthe oryzae,* is recognised by the paired rice nucleotide-binding leucine-rich repeat immune receptors OsRGA4/OsRGA5 through direct binding to an integrated heavy metal-associated (HMA) domain in OsRGA5. Here, we identify previously unknown host targets of AVR-Pia: four HMA domain-containing rice proteins, belonging to the HMA Isoprenylated Plant Proteins (HIPPs) and HMA Plant Proteins (HPPs). AVR-Pia interacted with all four proteins, both in vitro and in planta, and bound their HMA domains with varying affinities. The crystal structure of AVR-Pia in complex with the HMA domain of OsHPP09 revealed the molecular details of the binding interface. Structure-guided mutagenesis of OsHPP09 identified a single point mutation which prevents AVR-Pia binding, providing a foundation for targeted engineering of HMA domains to evade effector binding.

51 ## Introduction

52 The fungal pathogen *Magnaporthe oryzae* (syn. *Pyricularia oryzae*) is the causative agent of
53 rice blast, one of the most devastating diseases affecting cultivated rice worldwide[1,2]. *M.*
54 *oryzae* also causes severe yield losses in other cereals, including millets, barley and wheat,
55 threatening global food security[1].

56 To successfully colonise host plants, *M. oryzae* must evade plant defence responses and
57 manipulate host cellular pathways to its advantage. Central to infection is the secretion of a
58 large repertoire of effector proteins, many of which can be categorised into structural families[3].
59 In *M. oryzae,* the *Magnaporthe* AVRs and ToxB-like (MAX) effectors form the largest structural
60 family[4]. MAX effectors are defined by a conserved fold consisting of two β-sheets, each
61 composed of three antiparallel β-strands and stabilised by one or more disulphide bonds.
62 Despite this shared structure, there is little amino acid sequence similarity between MAX
63 effectors. They differ in surface properties and some carry variable N- and C-terminal
64 extensions, which can influence their folding pathway[5] and mediate interactions with host
65 proteins[3,6–9].

66 AVR-Pia is a MAX effector present in approximately 20% of rice-infecting *M. oryzae* isolates.
67 It is highly expressed during the biotrophic phase of host colonisation and contributes to
68 virulence on rice[4,7,10]. AVR-Pia can be recognised by the intracellular immune receptor
69 OsRGA5, a nucleotide-binding leucine-rich repeat (NLR) protein that functions together with
70 the helper NLR OsRGA4 to activate immune responses and restrict the spread of *M. oryzae*[11–
71 13]. Canonical plant NLRs consist of an N-terminal signalling domain, a central nucleotide-
72 binding domain and a C-terminal leucine-rich repeat domain[14]. However, many NLRs also
73 carry non-canonical integrated domains (IDs), thought to originate from host proteins targeted
74 by pathogen effectors[15]. These IDs, found across diverse plant species, are believed to
75 function as mimics or baits for effector recognition ("integrated decoy" model)[15–18]. Despite
76 sharing limited sequence similarity, both AVR-Pia and a second MAX effector, AVR1-CO39,
77 bind to the heavy metal-associated (HMA) ID of OsRGA5[11,12]. While this suggests that these
78 effectors may target host proteins containing HMA domains to promote disease, no host
79 targets of AVR-Pia or AVR1-CO39 have been identified, and their specific virulence functions
80 remain unknown.

81 The OsRGA5 HMA ID shares sequence similarity with a family of HMA domain-containing
82 metallochaperone-like proteins. The family can be subdivided into two groups: HMA domain-
83 containing Isoprenylated Plant Proteins (HIPPs) that carry a C-terminal CaaX isoprenylation

84 motif, and HMA domain-containing Plant Proteins (HPPs) that lack this motif[19,20]. The two
85 groups are collectively referred to hereafter as H(I)PPs. Isoprenylation, a post-translational
86 modification involving the covalent attachment of an isoprenoid lipid to the cysteine residue in
87 the CaaX motif, has been reported to facilitate membrane association[21]. Many HIPPs harbour
88 proline-rich regions between the HMA domain and the CaaX motif, potentially mediating
89 protein-protein interactions[19,22]. Typically, HMA domains feature a metal-binding MxCxxC
90 motif, implicating H(I)PPs in roles related to metal homeostasis[23,24]. However, approximately
91 a third of rice H(I)PPs lack one or both cysteines in their MxCxxC motif, suggesting functional
92 diversification beyond metal binding. H(I)PPs have undergone extensive expansion in
93 vascular plants, with approximately 100 members identified in rice[19,25–27]. Most remain
94 functionally uncharacterized, although several have been implicated in response to various
95 biotic and abiotic stresses[19,28–30]. Increasing evidence points to a broader role of H(I)PPs as
96 susceptibility factors in interactions with pathogens, pests, and viruses[27,31–41].

97 In cereals, H(I)PPs have been identified as susceptibility factors for *M. oryzae* infection[27,33,34].
98 A loss-of-function allele of *OsHIPP05* (*Pi21*) contributes to blast resistance in the field.
99 *OsHIPP20* is also a susceptibility gene; a loss-of-function mutation reduces the susceptibility
100 of rice to *M. oryzae*[27]. Some H(I)PPs are targeted by *M. oryzae* MAX effectors AVR-Pik and
101 APikL2[8,27,42]. AVR-Pik specifically interacts with members of a phylogenetic subclade of
102 OsH(I)PPs, referred to as clade A, including OsHIPP19, OsHIPP20, OsHPP03, and
103 OsHPP04[8,27]. The paired rice NLR proteins OsPik-1 and OsPik-2 mediate recognition of AVR-
104 Pik, which requires direct binding of the effector to an HMA ID in OsPik-1[43–45]. The HMA
105 domain of OsPik-1 belongs to the same phylogenetic clade as the H(I)PPs targeted by AVR-
106 Pik, reinforcing the idea that effector targets may serve as templates for domain integration
107 into NLRs.

108 Structural analyses of complexes between AVR-PikF or APikL2 and the HMA domains of their
109 HIPP targets or cognate NLR receptors have revealed a conserved binding interface centring
110 on β3 of the MAX fold and β4 of the HMA domain[8,42,45,46]. By contrast, the crystal structure of
111 AVR1-CO39 bound to the HMA ID of OsRGA5 revealed a markedly different interface
112 involving β2 of both AVR1-CO39 and OsRGA5-HMA[12]. NMR titration experiments, structural
113 modelling, and mutagenesis assays indicated that AVR-Pia binds OsRGA5-HMA at a similar
114 interface[12,13,47]. Additionally, the crystal structure of AVR-Pia in complex with Os-Pikp-HMA
115 revealed a similar binding interface, indicating that AVR-Pia binds different HMA domains in a
116 structurally similar manner[48]. The crystal structure of the MAX effector Pwl2 bound to
117 OsHIPP43 also revealed an interface involving β2 of the Pwl2 MAX fold and β2 of OsHIPP43-
118 HMA[9]. However, unlike AVR-Pia and AVR1-CO39, Pwl2 has a C-terminal extension,

119 comprising an α-helix and an unstructured region, which contributes significantly to HMA
120 binding[9]. Collectively, these structural studies underscore the remarkable diversity with which
121 MAX effectors have evolved to bind various HMA domain-containing proteins. They support
122 the hypothesis that AVR-Pia and AVR1-CO39 target distinct H(I)PPs through interfaces that
123 differ from those employed by other MAX effectors.

124 Here, we identified four OsH(I)PPs as specific interactors of AVR-Pia, none of which are bound
125 by the MAX effectors AVR1-CO39, AVR-Pik and Pwl2. Using biochemical and biophysical
126 approaches, we characterised the interaction between AVR-Pia and one of the interactors,
127 OsHPP09. The crystal structure of AVR-Pia/OsHPP09-HMA complex showed global similarity
128 to the AVR1-CO39/OsRGA5-HMA complex but revealed more extensive intermolecular
129 hydrogen bonding. Guided by the AVR-Pia/OsHPP09-HMA structure, we introduced a point
130 mutation in OsHPP09 which disrupts its interaction with AVR-Pia without compromising the
131 HMA fold.

132 Results

133 AVR-Pia interacts with rice H(I)PPs in Y2H screening

134 As AVR-Pia is recognised by OsRGA5 through direct binding to its HMA ID[11,13], we
135 hypothesised that AVR-Pia may target HMA domain-containing proteins to promote host
136 susceptibility. We conducted pairwise yeast two-hybrid (Y2H) assays, using a signal peptide-
137 deleted version of AVR-Pia (dSP-AVR-Pia, 20-85 aa) fused to the GAL4 activation domain
138 (AD) against a rice HMA domain library[49] comprising 78 rice H(I)PP HMA domains fused to
139 the GAL4 DNA binding domain (BD). Five HMA domains interacted with AVR-Pia: OsHPP09
140 (LOC_Os03g02070), OsHIPP41 (LOC_Os03g06080), OsHPP11 (LOC_Os04g45130),
141 OsHIPP14 (LOC_Os04g39320) and OsHIPP39 (LOC_Os03g02860) (**Fig. 1a,
142 Supplementary Fig. 1, Supplementary Table 1**). When paired with AVR-Pia, OsHPP09-
143 HMA conferred strong yeast growth on interaction-selective media, indicating a robust
144 interaction, while yeast growth for the remaining candidates was weaker.

145 We additionally tested the HMA library against the well-characterised MAX effectors Pwl2 and
146 AVR-PikD. Consistent with earlier publications, we observed dSP-Pwl2 (22-145 aa) interacting
147 with the HMA domain of OsHIPP43, and dSP-AVR-PikD (22-113 aa) interacting with the HMA
148 domains of OsHIPP19, OsHIPP20, and other phylogenetically related HMA domains[8,9,27,34]
149 (**Supplementary Fig. 1**), confirming the sensitivity of our screen.

150 In parallel, we performed an independent Y2H screen using a rice cDNA library. This identified
151 OsHIPP21 (LOC_Os09g09830) as a putative interactor of AVR-Pia (**Supplementary Table**
152 **1, Supplementary Table 2**).

153 For each interacting HMA domain, we next tested whether full-length (FL) proteins also bind
154 AVR-Pia in pairwise Y2H assays. Interestingly, interaction between AVR-Pia and FL OsH(I)PP
155 proteins was only observed for OsHPP09, OsHPP11 and OsHIPP21 (**Fig. 1a and**
156 **Supplementary Fig. 2**), despite confirmed expression of all proteins (**Supplementary Fig.**
157 **3a, 3b, 3c**). To exclude the possibility that the isoprenylation (CaaX) motif of studied FL HIPPs
158 affects nuclear localisation in yeast[21], we mutated the cysteine to serine (**Supplementary Fig.**
159 **3a, 3b**). However, OsHIPP14^{C187S}, OsHIPP39^{C190S} and OsHIPP41^{C152S} did not interact with
160 AVR-Pia in Y2H assays (**Supplementary Fig. 2**).

161 The HMA domains of OsHPP09 and OsHPP11 share 91.5 % and 74.6 % amino acid sequence
162 identity with OsHPP10 (LOC_Os10g36200) (**Supplementary Fig. 4**). Surprisingly, AVR-Pia
163 did not interact with OsHPP10-HMA nor the FL protein in Y2H assays (**Fig. 1a**). By contrast,
164 OsHIPP21-HMA shares only 30-40% sequence identity with the HMA domains of the three
165 OsHPPs (**Supplementary Fig. 4**), and while the HMA domain of OsHIPP21 did not interact
166 with AVR-Pia, FL OsHIPP21 did. Taken together, these results suggest that AVR-Pia binds
167 and potentially targets OsHPP09, OsHPP11, and OsHIPP21.

168 Previous work classified MAX effectors into 20 structural groups[6]. MAX58 belongs to the same
169 group as AVR-Pia, but differs in surface properties[6]. dSP-MAX58 (20-86 aa) did not interact
170 with any of the tested OsH(I)PPs in Y2H assays (**Fig. 1a, Supplementary Fig. 1**), although
171 the effector protein was expressed (**Supplementary Fig. 3c**), suggesting that, despite their
172 shared structural fold, effectors with distinct surface properties target different host proteins.

173 **AVR-Pia interacts with rice H(I)PPs in planta**

174 To test whether AVR-Pia and the four OsH(I)PPs interact in planta, we performed split-
175 luciferase complementation assays in *Nicotiana benthamiana*. 3xFlag-CLuc-OsH(I)PP FL
176 proteins were co-expressed with 3xHA-NLuc-dSP-AVR-Pia or 3xHA-NLuc-dSP-MAX58. Co-
177 expression of FL OsHPP09, OsHPP11, and OsHIPP21 with AVR-Pia led to high
178 luminescence levels, exceeding those observed for the positive control OsRGA5$_{Cter}$ (883-1116
179 aa, including the HMA ID) (**Fig. 1b**). Strikingly, a strong luminescence signal was observed for
180 OsHPP10/AVR-Pia, within a similar range to OsHPP09 and OsHPP11 and exceeding
181 OsHIPP21 (**Fig. 1b**). Consistent with the Y2H results, no interaction was observed in planta
182 between AVR-Pia and other tested FL OsHIPPs, including OsHIPP14, OsHIPP39 and
183 OsHIPP41 (**Fig. 1b**). MAX58 showed no interaction with any of the tested OsH(I)PPs (**Fig.**
184 **1b**). Expression of all proteins was confirmed by immunoblot analyses (**Supplementary Fig.**

185 **5**). These data demonstrate that AVR-Pia interacts in planta with OsHPP09, OsHPP10,
186 OsHPP11 and OsHIPP21.

187 **AVR-Pia interacts with the HMA domains of OsHPP09, OsHPP10, OsHPP11 and**
188 **OsHIPP21 in vitro with varying affinities**

189 Recombinant AVR-Pia and HMA domains were produced and purified from *E. coli*
190 (**Supplementary Fig. 6**). We first tested for interaction between purified OsHPP09-HMA and
191 AVR-Pia using analytical size exclusion chromatography. When analysed alone, the peak
192 elution volumes for AVR-Pia and OsHPP09-HMA were 15.3 ml and 13.0 ml, respectively (the
193 latter is consistent with dimerisation, as reported for other HMA domains in solution[12,45]).
194 Following incubation with OsHPP09-HMA (1:1 effector:HMA ratio), the peak elution volume of
195 AVR-Pia shifted to 12.7 ml, consistent with formation of an AVR-Pia/OsHPP09-HMA complex
196 (**Supplementary Fig. 7**). The co-elution of the two proteins was supported by SDS-PAGE
197 analysis of elution fractions (**Supplementary Fig. 7**).

198 To determine the affinity with which AVR-Pia binds to the HMA domains of OsHPP09,
199 OsHPP10, OsHPP11 and OsHIPP21, we used isothermal titration calorimetry (ITC). Titration
200 of AVR-Pia into a solution containing any of the purified HMA domains resulted in negative
201 peaks in the titration curve (**Fig. 2, Supplementary Fig. 8**), indicating an exothermic binding
202 interaction. Dissociation constant (K_D) values were determined from binding isotherms (**Fig.**
203 **2, Supplementary Fig. 8**) fitted to a single site model.

204 AVR-Pia bound to OsHPP09-HMA with an apparent K_D of 115 nM (**Fig. 2**). Despite differing
205 in just six amino acids, AVR-Pia bound OsHPP10-HMA with significantly lower affinity, with
206 an apparent K_D of 5.26 μM. The binding affinities of AVR-Pia and OsHPP11-HMA or
207 OsHIPP21-HMA fell between these two extremes, with apparent K_Ds of 772 nM and 1.29 μM,
208 respectively (**Fig. 2, Supplementary Fig. 8, Supplementary Fig. 9, Supplementary Table**
209 **3**). The apparent K_Ds, determined by ITC, for the interactions between OsRGA5-HMA and
210 AVR-Pia or AVR1-CO39 were previously reported as 7.8 μM[13] and 5.1 μM[12], respectively.

211 **AlphaFold Multimer models cannot differentiate between HMA domains which are**
212 **bound by AVR-Pia and those which are not**

213 Several studies have used AlphaFold Multimer to distinguish interacting from non-interacting
214 pairs of effectors/host proteins[27,50,51]. We therefore tested whether structural models of AVR-
215 Pia in complex with experimentally verified interactors (OsHPP09-HMA, OsHPP10-HMA,
216 OsHPP11-HMA and OsHIPP21-HMA) showed differences, either in the models themselves
217 or in the associated confidence metrics, compared to structural models of AVR-Pia with non-
218 interacting HMA domains. We modelled AVR-Pia/HMA complexes using AlphaFold2 and

219 AlphaFold3. High confidence models were obtained for all AVR-Pia/HMA pairs except AVR-
220 Pia/OsHIPP42-HMA using AlphaFold2 (**Supplementary Fig. 10**) and AVR-Pia/OsHIPP41-
221 HMA using AlphaFold3 (**Supplementary Fig. 11**). For the AlphaFold2 models, interface
222 analysis with qtPISA revealed a tendency towards increased interface area for AVR-Pia-
223 interacting HMA domains compared to non-interacting HMA domains. (**Supplementary Fig.
224 10)**. By contrast, there were no significant differences for AlphaFold3 models (**Supplementary
225 Fig. 11**). Overall, AlphaFold could not clearly differentiate between HMA domains bound or
226 not bound by AVR-Pia.

227 **AVR-Pia-H3 does not interact with OsHPP09, OsHPP10, OsHPP11 and OsHIPP21**

228 Some rice-infecting *M. oryzae* isolates carry an allele of AVR-Pia, AVR-Pia-H3, which contains
229 two non-synonymous polymorphisms (F24S and T46N)[11] (**Supplementary Fig. 12**). These
230 polymorphisms interfere with OsRGA5-HMA binding and allow evasion of OsRGA4/OsRGA5-
231 mediated immunity[11,13]. Pairwise Y2H assays revealed that AVR-Pia-H3 failed to interact with
232 FL OsHPP09, OsHPP10, OsHPP11 and OsHIPP21 or their HMA domains (**Fig. 3a**). In planta
233 split-luciferase complementation assays gave only weak luminescence signals for AVR-Pia-
234 H3 with OsH(I)PPs, comparable to the negative control pairs $OsRGA5_{Cter}$/AVR-Pia-H3 and
235 OsHPP09/MAX58, and markedly lower than the positive control OsHPP09/AVR-Pia (**Fig. 3b**).
236 Protein expression in yeast and in planta was confirmed by immunoblot (**Supplementary Fig.
237 3c and 13**). Analysis of a 1:1 effector:HMA mixture of purified recombinant AVR-Pia-H3 and
238 OsHPP09-HMA by analytical size exclusion chromatography showed no co-elution of the two
239 proteins, indicating that they did not form a stable complex in vitro (**Fig. 3c**).

240 Together, these data indicate that the F24S and T46N polymorphisms that disrupt binding of
241 AVR-Pia to the HMA ID of OsRGA5 also interfere with binding to its candidate host targets.

242 **AVR1-CO39 does not interact with OsHPP09, OsHPP10, OsHPP11 and OsHIPP21**

243 As the HMA ID of OsRGA5 also binds the MAX effector AVR1-CO39[11,12], we tested whether
244 AVR1-CO39 binds to the same H(I)PPs as AVR-Pia. dSP-AVR1-CO39 (22-89 aa) did not
245 interact with FL OsHPP09, OsHPP10, OsHPP11 or OsHIPP21, nor their HMA domains, in
246 Y2H, whereas interaction with $OsRGA5_{Cter}$ was confirmed (**Fig. 4a**). Effector expression was
247 confirmed by immunoblot (**Supplementary Fig. 3c**).

248 In split-luciferase complementation assays, we observed weak luminescence for AVR1-CO39
249 with FL OsHPP09, OsHPP10 and OsHPP11, similar to the luminescence observed with
250 $OsRGA5_{Cter}$ but substantially lower than the level observed for AVR-Pia/OsHPP09 (**Fig. 4b**).
251 Consistent with the Y2H results, no interaction was detected between FL OsHIPP21 and
252 AVR1-CO39, similar to the negative control OsPi21/AVR1-CO39 (**Fig. 4b**). Protein expression
253 was validated by immunoblot (**Supplementary Fig. 14**). Analytical size-exclusion

254 chromatography with purified proteins further supported the absence of complex formation
255 (**Fig. 4c**).

256 Collectively, these results suggest that, while AVR1-CO39 and AVR-Pia are both recognised
257 by the same HMA ID in OsRGA5, they do not bind the same H(I)PPs.

258 **AVR-Pia interacts with a distinct group of H(I)PPs to AVR-Pik and Pwl2**

259 Previous studies have shown that the MAX effectors AVR-PikC, AVR-PikD and Pwl2 target
260 H(I)PPs[8,9,27,34]. However, dSP-AVR-PikC (22-113 aa), dSP-AVR-PikD (22-113 aa) and dSP-
261 Pwl2 (22-145 aa) did not bind to the AVR-Pia interactors OsHPP09, OsHPP10, OsHPP11 and
262 OsHIPP21 in Y2H assays (**Fig. 5a**), while we confirmed the known interactions of AVR-
263 PikC/AVR-PikD with OsHIPP19/OsHIPP20, and Pwl2 with OsHIPP43 (**Fig. 5a**). Interestingly,
264 AVR-Pia interacted with FL OsHIPP19 under low-stringency Y2H conditions (**Fig. 5a**).

265 The lack of interaction between AVR-PikC and AVR-PikD with FL OsHPP09, OsHPP10,
266 OsHPP11 and OsHIPP21 was validated through split-luciferase complementation assays
267 (**Fig. 5b**). AVR-Pia showed an interaction with OsHIPP19 similar to that observed for AVR-
268 PikD, and a weaker interaction with OsHIPP20 (**Fig. 5b**). Co-expression of Pwl2 with
269 OsHPP09, OsHPP10, OsHPP11 and OsHIPP21 resulted in very weak luminescence. Protein
270 expression was confirmed by immunoblot (**Supplementary. Fig. 15**).

271 Together, our findings indicate that the HMA domains bound by AVR-Pia are not targeted by
272 AVR-Pik and Pwl2, suggesting that despite sharing a conserved MAX effector fold, these
273 effectors target different H(I)PPs.

274 **The crystal structure of the AVR-Pia/OsHPP09-HMA complex reveals interface contacts**
275 **underpinning high affinity binding**

276 To understand the structural basis of the interaction between AVR-Pia and OsHPP09-HMA,
277 we purified and crystallised the effector/HMA complex. Needle-like crystals were obtained in
278 commercial screens and subsequent optimisation of conditions resulted in crystals suitable for
279 diffraction studies. X-ray diffraction data were collected at the European Synchrotron
280 Radiation Facility (ESRF) to a resolution of 1.65 Å. The structure was solved by molecular
281 replacement, refined and validated as described in the Materials and Methods. Data collection,
282 processing and refinement statistics are presented in **Supplementary Table 4**. The final
283 refined model has been deposited in the Protein Data Bank (PDB accession code 9RSV).

284 As expected, OsHPP09-HMA adopts the well-characterised HMA domain fold, consisting of a
285 four-stranded antiparallel β-sheet and two α-helices arranged with βαββαβ topology (**Fig. 6**).
286 Structures of AVR-Pia have previously been determined by NMR spectroscopy[4,52] (PDB

287 accession codes 2MYW, 2N37) and X-ray crystallography[48] (PDB accession code 6Q76;
288 complex with Pikp-1 HMA ID). The structure of AVR-Pia determined here is highly similar
289 (RMSD of 0.357 Å to 6Q76, 0.951 Å to 2MYW, and 1.690 Å to 2N37) and adopts the six-
290 stranded β-sandwich fold characteristic of the MAX effectors (**Fig. 6**)[4,6].

291 Globally, the AVR-Pia/OsHPP09-HMA complex resembles the previously determined
292 structures of AVR-Pia/OsPikp-1-HMA (PDB 6Q76) and AVR1-CO39/OsRGA5-HMA (PDB
293 5ZNG) (**Supplementary Fig. 16**). The AVR-Pia/OsHPP09-HMA interface area is 521.7Å^2,
294 fractionally larger than AVR-Pia/OsPikp-HMA (460.7 Å^2) and AVR1-CO39/OsRGA5-HMA
295 (492.8 Å^2) (**Supplementary Table 5**). In all three complexes, β2 of the MAX effector is aligned
296 with β2 of the HMA domain, forming an antiparallel β-sheet comprising β6, β1, and β2 of the
297 MAX effector and the four-stranded β-sheet of the HMA domain (**Supplementary Fig. 16a**),
298 with hydrogen bonding between adjacent β-strands (**Supplementary Fig. 16b**).

299 In contrast to AVR-Pia/OsPikp-HMA and AVR1-CO39/OsRGA5-HMA, where the interface is
300 dominated by main chain hydrogen bonding, in OsHPP09-HMA/AVR-Pia, the side chains of
301 multiple residues in α1 of the HMA domain form intermolecular hydrogen bonds with the
302 effector. The side chains of OsHPP09^{E16} and OsHPP09^{K19} form hydrogen bonds with the
303 peptide backbone of AVR-Pia^{L38} (**Supplementary Fig. 16c**). OsPikp-1^{R203} is in the
304 corresponding position to OsHPP09^{K19}, however it is OsPikp-1^{R226}, in the β2-β3 loop, which
305 forms an analogous hydrogen bond with AVR-Pia^{L38} (**Supplementary Fig. 16c**). OsRGA5-
306 HMA has a basic residue (R1012) at the corresponding position to OsHPP09^{K19}, and the side
307 chain of OsRGA5-HMA^{R1012} is orientated towards the AVR1-CO39^{D35} side chain, however the
308 distance between them (4.1 Å) is greater than the 4 Å cutoff typically used when considering
309 salt bridge interactions (**Supplementary Fig. 16c**). At the start of β2, the OsHPP09^{D33} side
310 chain forms salt bridge interactions with the AVR-Pia^{R43} side chain (**Supplementary Fig. 16d**).
311 This aspartate residue is conserved in both OsPikp-HMA (D217), where it similarly forms a
312 salt bridge with AVR-Pia^{R43}, and OsRGA5-HMA (D1026), where it forms an indirect, water-
313 mediated contact with the backbone of AVR1-CO39^{T41} (**Supplementary Fig. 16d**). The
314 OsHPP09^{Q20} side chain forms hydrogen bonds with the side chain hydroxyl of AVR-Pia^{Y41}
315 (**Supplementary Fig. 16e**). The serine in the corresponding position in OsPikp-HMA (S204)
316 forms a water-mediated contact with the side chain hydroxyl of AVR-Pia^{Y41} (**Supplementary**
317 **Fig. 16e**). Finally, towards the C-terminal end of OsHPP09-α1, the side chain of OsHPP09^{D28}
318 forms a salt bridge with AVR-Pia^{R23} (**Supplementary Fig. 16f**). By contrast, the corresponding
319 amino acid in OsPikp-1, OsPikp-1^{S212}, forms a hydrogen bond with the side chain hydroxyl of
320 AVR-Pia^{Y85} (**Supplementary Fig. 16f**). Overall, the increased number of intermolecular

321 hydrogen bonds in the AVR-Pia/OsHPP09-HMA structure compared to the structure of AVR1-
322 CO39/OsRGA5-HMA likely explains the difference in binding affinities.

323 To validate the interface observed in the crystal structure, NMR titration with ^{1}H-^{15}N-HSQC
324 NMR 2D spectra of ^{15}N-labelled AVR-Pia alone and in the presence of unlabelled OsHPP09-
325 HMA were performed. HSQC spectra for ^{15}N-labelled AVR-Pia had previously been collected,
326 and the resonances of amide cross-peaks had been assigned[4]. Binding of AVR-Pia to
327 OsHPP09-HMA alters the chemical environment of the amino acids located at the binding
328 interface, resulting in a change in the chemical shift observed for those amino acids in the ^{15}N
329 HSQC spectra. The ^{15}N HSQC spectra of the complex AVR-Pia with unlabelled OsHPP09-
330 HMA were reassigned using ^{15}N,^{13}C-AVR-Pia and two- and three-dimensional NMR
331 experiments **(Supplementary Fig. 17).** Depending on the exchange rate constant (kex)
332 between the bound and unbound states and on the frequency difference ($\Delta\omega$) between the
333 corresponding resonances in these two states, different NMR exchange regimes occur. NMR
334 titration showed that the AVR-Pia:OsHPP09-HMA complex was in slow exchange with kex
335 $<< \Delta\omega$ since separate resonances appeared for individual species **(Supplementary Fig. 18)**.
336 An NMR slow exchange regime indicates a relatively high affinity (<0.1 μM) between the two
337 proteins. The chemical shift perturbations of AVR-Pia in the absence and presence of
338 OsHPP09-HMA were calculated, and significant changes in chemical shift ($> \overline{\Delta\delta} + 1\sigma$) were
339 observed for multiple residues in β2 and β3 of AVR-Pia, consistent with the interface in the
340 crystal structure **(Supplementary Fig. 19)**.

341 **Replacement of OsHPP09^{E16} with alanine or arginine disrupts AVR-Pia binding**

342 We aimed to identify point mutations in OsHPP09-HMA that interfere with AVR-Pia binding.
343 First, we selected residues whose side chains contribute intermolecular hydrogen bonds or
344 salt bridges and mutated these to alanine (E16A, K19A, Q20A, D28A, D33A) and, for acidic
345 residues, to arginine (E16R, D28R, D33R). D33 is conserved in OsHPP09, OsHPP10,
346 OsHPP11, and in the HMA IDs of Pikp-1 (D217) and RGA5 (D1026) (**Supplementary Fig.
347 16D**). By contrast, the corresponding residue in Pikm-HMA, which does not bind AVR-Pia[48],
348 is histidine. We therefore also mutated D33 to histidine. Second, we used FoldX[53] to predict
349 the effect of mutating each interface residue in OsHPP09-HMA to all other amino acids. Based
350 on the calculated difference of interaction free energy (ΔΔG) upon mutation, we made three
351 further mutations: K19W, I35K, and A37W.

352 Introduction of the point mutations E16A, E16R, D28A, D28R and I35K in OsHPP09 resulted
353 in a complete loss of interaction with AVR-Pia in Y2H experiments (**Fig. 7a**). The remaining
354 mutations (i.e., K19A, K19W, D33A, D33H, D33R, A37W) with the exception of Q20A, led to

355 reduced yeast growth on selective media suggesting a weakening of the interaction compared
356 to the wildtype OsHPP09/AVR-Pia pair (**Fig. 7a**). Immunoblot analysis revealed that the K19A,
357 K19W and I35K mutants exhibited lower protein expression levels, while all other mutant
358 constructs showed similar expression to wildtype OsHPP09 (**Supplementary Fig. 3d**).

359 To assess the effect of the mutations in the context of the full-length protein in planta, we
360 performed split-luciferase complementation assays. The E16A and E16R mutants showed
361 significantly reduced interaction with AVR-Pia, while the I35K mutant completely lost its ability
362 to interact with AVR-Pia, consistent with the Y2H results (**Fig. 7b**). In contrast, the D28A and
363 D28R mutations, which abolished interaction in Y2H assays, had only a minor effect on the
364 interaction with AVR-Pia in planta, similar to the other tested mutants (**Fig. 7b**). Immunoblot
365 analysis demonstrated that all proteins were expressed at comparable levels in planta
366 (**Supplementary Fig. 20**).

367 Next, we aimed to establish whether the E16A, E16R, D33H and I35K mutations affect the
368 structure of the HMA domain. Mutated HMA domains were produced in *E. coli*, purified to
369 homogeneity, and molecular weights were confirmed by intact mass spectrometry. Circular
370 dichroism (CD) spectra for OsHPP09^{E16A}-HMA, OsHPP09^{E16R}-HMA and OsHPP09^{D33H}-HMA
371 were comparable to the spectra for wildtype OsHPP09-HMA with features characteristic of α-
372 helices (negative peaks around 222 nm and 208 nm, positive peak around 193 nm) and β-
373 sheets (negative peak around 218 nm, positive peak around 195 nm) consistent with the HMA
374 domain fold (**Fig. 7c**). By contrast, OsHPP09^{I35K}-HMA showed features of disorder (low
375 ellipticity above 210 nm and a negative peak around 200 nm) (**Fig. 7c**), suggesting that the
376 lack of AVR-Pia binding to the I35K mutant is likely due to disruption of the HMA domain fold.

377 We obtained ^{1}H-^{15}N-HSQC NMR spectra of ^{15}N-AVR-Pia in the presence of (unlabelled) HMA
378 domains of OsHPP09^{E16A}, OsHPP09^{E16R}, and OsHPP09^{D33H}. The spectra of ^{15}N-AVR-Pia with
379 OsHPP09^{D33H}-HMA was highly similar to the spectra of ^{15}N-labelled AVR-Pia with WT
380 OsHPP09-HMA (**Fig. 7d**, **Supplementary Fig. 21**), although the exchange regime changes
381 at certain cross-peaks, suggesting lower binding affinity. By contrast, the spectra of ^{15}N-AVR-
382 Pia with OsHPP09^{E16A} or OsHPP09^{E16R} showed no chemical shift perturbation and largely
383 superimposed with the spectra of ^{15}N-AVR-Pia alone (**Fig. 7d**, **Supplementary Fig. 22**,
384 **Supplementary Fig. 23**). Taken together, these results demonstrate that E16A and E16R
385 mutations block AVR-Pia binding without disrupting the HMA fold, while the I35K mutation
386 interferes with correct folding of the HMA domain.

387 ## Discussion

388 In the present study, we found that the *M. oryzae* MAX effector AVR-Pia binds to the HMA
389 domains of four rice H(I)PPs: OsHPP09, OsHPP10, OsHPP11, and OsHIPP21. Neither AVR-
390 Pik nor Pwl2 interacts with these H(I)PPs, demonstrating that AVR-Pia binds a distinct group
391 of H(I)PPs to those previously identified as MAX effector targets. Indeed, AVR-Pik interacts
392 with multiple H(I)PPs within a large phylogenetic clade (referred to as "clade A")[27], while Pwl2
393 interacts specifically with OsHIPP43 and its homologs from other grass species[9].

394 Strikingly, the interactions between each of these three MAX effectors and HMA domains
395 involve distinct interfaces. In the crystal structures of AVR-Pia/OsHPP09-HMA and
396 Pwl2/OsHIPP43-HMA, β2 of the core MAX fold and β2 of the HMA domain are aligned in an
397 antiparallel orientation[9], forming an antiparallel β-sheet comprising the four β-strands of the
398 HMA domain and β2, β1, and β6 of the MAX fold. When the HMA domains are superposed,
399 the relative positions of β2 of the MAX fold of Pwl2 and AVR-Pia are very similar
400 (**Supplementary Fig. 24**). However, the other β-strands of Pwl2 are shifted compared to AVR-
401 Pia, enabling residues in β3, β4, and the β3-β4 loop of the MAX fold to contribute to the HMA-
402 binding interface. By contrast, in the OsHIPP19-HMA/AVR-PikF complex, an antiparallel β-
403 sheet forms from the four β-strands of the HMA domain and β3, β4 and β5 of the MAX fold,
404 mediated by hydrogen bonding between β3 of AVR-PikF and β4 of HIPP19-HMA[8].
405 Furthermore, while AVR-Pia consists solely of the core MAX fold, AVR-Pik has an
406 unstructured extension at the N-terminus, while in Pwl2 the characteristic MAX fold is followed
407 by an α-helix and a C-terminal unstructured region, and these extensions are involved in HMA
408 binding (**Supplementary Fig. 24**). $Pwl2^{E89}$, in the α-helix, forms a hydrogen bond with
409 $OsHIPP43\text{-}HMA^{K51}$, while the C-terminal unstructured segment of Pwl2 extends across the
410 HMA domain, forming an extensive interface involving both hydrogen bonds and π-stacking
411 interactions. Similarly, the N-terminal extension of AVR-Pik forms multiple hydrogen bonds
412 with residues in β3, β2, and the β2-β3 loop of OsHIPP19-HMA. The interface in the AVR-
413 Pia/OsHPP09-HMA complex is smaller than in AVR-PikF/OsHIPP19-HMA and
414 Pwl2/OsHIPP43-HMA (521.6 $Å^2$ compared to 1044.3 $Å^2$ and 1965.2 $Å^2$, respectively), and is
415 formed almost exclusively by residues in β2 of the core MAX fold.

416 It is highly interesting that at least three MAX effectors have evolved to bind HMA domains in
417 different ways. This highlights how structural variation within this effector family can underpin
418 different interactions with host targets. It is unknown whether the interactions of AVR-Pia,
419 AVR-Pik, and Pwl2 with OsH(I)PPs lead to similar outcomes (redundancy) or if each binding
420 event has a distinct and specific impact on plant susceptibility and/or fungal virulence.

421 While AVR-Pia, AVR-Pik, and Pwl2 all target OsH(I)PPs, the MAX effector AvrPiz-t has been
422 reported to interact with a range of host proteins[54,55]. From a structural perspective, it is unclear
423 how a single MAX effector binds to such diverse targets. However, this suggests that MAX
424 effectors may target many different host proteins and processes during infection.

425 AVR-Pia is recognised by the paired rice NLR immune receptors OsRGA5 and OsRGA4
426 through direct binding of the effector to the non-canonical HMA domain integrated into
427 OsRGA5[11]. Such non-canonical domains are hypothesised to have originated in effector host
428 targets and were incorporated into NLR proteins to function as effector "sensors"[15]. Consistent
429 with this, the crystal structure of AVR-Pia/OsHPP09 revealed that AVR-Pia binds OsHPP09-
430 HMA and OsRGA5-HMA through similar interfaces[13]. Interestingly, the F24S and T46N
431 polymorphisms of AVR-Pia-H3 interfered with binding to both OsRGA5-HMA and the
432 candidate OsH(I)PP targets, in contrast to naturally-occurring polymorphisms in AVR-Pik
433 which prevent binding to the HMA ID of Pikp-1 without disrupting interaction with the HMA
434 domains of OsH(I)PP19 and OsH(I)PP20[8,27].

435 AVR1-CO39 is also recognised by direct binding to the HMA ID of OsRGA5. However, AVR1-
436 CO39 did not interact with the same OsH(I)PPs as AVR-Pia. AVR1-CO39 also did not interact
437 with the "clade A" OsH(I)PPs bound by AVR-PikD[27]. AVR1-CO39 is broadly absent from rice-
438 infecting isolates of *M. oryzae*[7,56,57] and its loss has potentially contributed to a host shift from
439 foxtail millet (*Setaria* sp.) to rice. It is therefore possible that AVR1-CO39 has evolved to target
440 H(I)PPs from other grass species, and does not interact with those present in rice.

441 Interestingly, phylogenetic analysis based on HMA domains clusters OsRGA5-HMA with the
442 H(I)PPs targeted by AVR-Pik and the HMA ID of OsPik-1, and not with OsHPP09, OsHPP10,
443 OsHPP11, and OsHIPP21[27]. This suggests that the RGA5-ID did not arise through duplication
444 and integration of these AVR-Pia candidate targets, but instead from another H(I)PP. We
445 observed interaction between AVR-Pia and FL OsHIPP19, but not with the HMA domain
446 alone, in low stringency Y2H experiments and split-luciferase assays. This suggests that the
447 C-terminal part of OsHIPP19 contributes to AVR-Pia binding and merits further study.

448 A previous study reported that AVR-Pia binds OsRGA5-HMA with a K_D of 7.8 μM[13]. This is
449 comparable to the binding affinity of AVR-Pia to OsHPP10-HMA, but at least one order of
450 magnitude weaker than the AVR-Pia/OsHPP09-HMA interaction. This higher affinity can be
451 explained by the number of intermolecular hydrogen bonds and salt bridges at the AVR-
452 Pia/OsHPP09 interface; available structures of AVR1-CO39/OsRGA5-HMA and AVR-
453 Pia/OsPikp-HMA, combined with modelling approaches, suggest that the AVR-Pia/OsRGA5-
454 HMA interface likely involves fewer intermolecular contacts. A similar pattern was reported for

455 AVR-Pik/HMA interactions; surface plasmon resonance experiments showed that AVR-PikD
456 interacts with the HMA domain of OsHIPP19 with higher affinity than the HMA ID of OsPik-1[8].
457 It is important to note that these binding affinities are determined in vitro using purified HMA
458 domains. These experiments therefore lack the biological context of the FL protein or the plant
459 cell environment.

460 H(I)PPs, which form extensive families in plants[19,25,26], have been reported to be involved in
461 intracellular metal transport and homeostasis, responses to cold and drought stress, and
462 heavy metal tolerance. In addition to the interactions between *M. oryzae* MAX effectors and
463 OsH(I)PPs, there are multiple examples of plant H(I)PPs targeted by proteins from diverse
464 pests and pathogens. For example, the putative effector RsMf8HN from the necrotrophic
465 fungus *Rhizoctonia solani* interacts with OsHIPP28[38], while a HIPP from sugarcane (ScPi21)
466 is a target for the *Fusarium sacchari* effector Fs00367[35]. CsHIPP03 was identified by Y2H
467 screening as an interactor of SDE34, an effector secreted by the phloem-colonising bacteria
468 *Candidatus* Liberibacter asiaticus[40]. A root-knot nematode (*Meloidogyne graminicola*) effector
469 binds rice OsHPP04 and suppresses the flg22-induced ROS burst[36]. Finally, the potato mop-
470 top virus movement protein interacts with NbHIPP26 to promote systemic spread of the virus[31].
471 Together, these results suggest that the manipulation of H(I)PPs is required for successful
472 infection by diverse pests and pathogens. However, little is known about the molecular
473 mechanisms through which H(I)PPs affect plant resistance and/or susceptibility.

474 HMA domains typically coordinate metal ions via two cysteine residues in an MxCxxC motif.
475 Intriguingly, the metal-binding motif is degenerate in all four HMA domains bound by AVR-Pia,
476 with both cysteines replaced by other amino acids (MTDEKT in OsHPP09, MTDDKI in
477 OsHPP10, MSDTKM in OsHPP11, and MTDERK in OsHIPP21), indicating the absence of
478 metal-binding. Consistent with this, no electron density suggestive of bound metal ions was
479 observed in the OsHPP09-HMA/AVR-Pia crystal structure. Interestingly, OsHPP09^{E16}, which
480 is important for AVR-Pia binding, is located in the degenerate metal binding motif. Of the "clade
481 A" H(I)PPs bound by AVR-Pik, some contain an intact MxCxxC motif, while others, such as
482 OsHIPP19 and OsHIPP20, lack one or both cysteine residues. OsHIPP43 has an intact
483 MxCxxC motif, though it is unknown whether it binds metal ions in planta. In cases where HMA
484 domains lack a complete MxCxxC motif, and presumably also the capacity to bind metals, the
485 functions of the H(I)PPs are particularly intriguing. Functional diversification, beyond metal
486 transport and homeostasis, may have been facilitated by the stable core fold of the HMA
487 domain supporting diversification of surface properties to deliver new functions. Protein
488 prenylation can affect subcellular localisation, protein stability, and protein-protein
489 interactions[58]. For some HIPPs, the C-terminal CaaX isoprenylation motif has been shown to

drive localisation to plasmodesmata. Further investigation is required to establish the localisation and function of the AVR-Pia interactors in planta.

Pathogens require certain host factors to establish a successful infection, with the underlying genes typically referred to as susceptibility (S) genes. Previous studies have shown that *OsHIPP05* (*Pi21*) and *OsHIPP20* are S genes for blast infection; *oshipp05* and *oshipp20* CRISPR-Cas9 knockout plants exhibited increased blast resistance compared to WT plants [27,33,34,59–61]. Further, a recent study reported that overexpression of barley (*Hordeum vulgare*) *HvHIPP43* increased susceptibility to *M. oryzae,* suggesting that *HvHIPP43* may also be an S gene[34]. Other plant H(I)PPs are also S genes for different pests and pathogens; *Arabidopsis thaliana* plants carrying loss-of-function mutations in *AtHIPP27* or *AtHMAD* (also known as *AtHIPP40*[29]) exhibited reduced susceptibility to the beet cyst nematode *Heterodera schachtii*[32] and the bacterial pathogen *Pseudomonas syringae*[41], respectively. Silencing of *TaHIPP1* in wheat reduced sporulation of the wheat stripe rust fungus *Puccinia striiformis* f. sp. *tritici*[39]. *OsHPP09*, *OsHPP10*, *OsHPP11,* and/or *OsHIPP21* may also be S genes for rice blast disease, and deletion of these genes may increase blast resistance.

Knocking out S genes has the potential to confer durable resistance, but can cause undesirable pleiotropic effects on plant growth and development[62–65]. Base editing offers a more precise alternative, allowing single amino acid changes that minimise disruption of protein function[66]. While the functions of OsHPP09, OsHPP10, OsHPP11, and OsHIPP21, and the consequences of AVR-Pia binding remain unknown, the virulence function of the MAX effector Pwl2 depends on interaction with OsHIPP43[34]. Altering effector targets to block effector binding could compromise the virulence function of effectors without compromising the folding or endogenous function of the host protein. However, it is crucial to verify that such mutations do not interfere with the folding and function of the host targets before commencing time-consuming and costly base editing experiments in plants.

In summary, we have characterised the interactions between AVR-Pia and a novel subset of HMA domain-containing rice proteins. Biophysical and structural analyses guided mutagenesis of these effector targets and identified a mutation that blocks effector binding without compromising structural integrity of the HMA domain. This provides a foundation for targeted modification of these proteins for enhanced disease resistance.

520 # Methods

521 ## Cloning

522 The coding sequences (CDS) of *OsH(I)PPs*, including the stop codon, were synthesised by
523 Twist Bioscience. The CDS of *OsHIPP14*, *OsPi21*, *OsHIPP19*, *OsHIPP21,* and *OsHPP09*
524 were codon-optimised to enable synthesis.

525 For Y2H and split luciferase experiments, synthesised *OsH(I)PP* genes were used as template
526 for amplification with primers containing *attB1* and *attB2* recombination sites (**Supplementary**
527 **Table S6**) and Phusion High-Fidelity DNA Polymerase (Thermo Fisher Scientific). Resulting
528 PCR products were subsequently introduced into the pDONR207 vector (Invitrogen) via
529 Gateway® BP recombination (Thermo Fisher Scientific). Entry constructs for the MAX
530 effectors dSP-AVR-Pia[15], dSP-AVR1-CO39[12], dSP-AVR-PikD[47] and dSP-Pwl2[13] were
531 previously published. The dSP-AVR-PikC fragment was amplified from pCambia1300_dSP-
532 AVR-PikC[45] and dSP-MAX58 from a synthesised gene, both using primers containing *attB1*
533 and *attB2* recombination sites (Supplementary Table S6) and Phusion High-Fidelity DNA
534 Polymerase (Thermo Fisher Scientific). Resulting PCR products were cloned into the
535 pDONR207 vector (Invitrogen) via Gateway® BP recombination (Thermo Fisher Scientific).

536 For recombinant protein production in *E. coli,* synthesised genes were used as templates for
537 PCR amplification of HMA domains (**Supplementary Table S1**) with primers containing *Bpi*I
538 restriction sites (**Supplementary Table S6**) using CloneAmp™ HiFi PCR Premix (Clontech
539 Laboratories). Resulting PCR products were introduced into pICH41308 (Addgene #47998[67])
540 by Golden Gate assembly[68] to generate level 0 CDS modules. The CDS of OsHIPP21-HMA
541 was codon-optimised for *E. coli* expression and supplied with appropriate overhangs and
542 restriction sites for direct assembly into the vector pICH41308 without PCR amplification. Level
543 0 CDS modules were used in Golden Gate reactions with the pOPIN-GG vector pPGN-C
544 (Addgene #174578[69]) and the level 0 module pICSL30015 (Addgene #174582[69]) to generate
545 *E. coli* expression constructs with a cleavable N-terminal 6xHis-MBP tag.

546 Site-directed mutagenesis of OsHPP09-HMA for Y2H, split luciferase, and recombinant
547 protein production was performed using a QuikChange Site-Directed Mutagenesis Kit
548 (Agilent). Prenylation motif mutations (*OsHIPP14*^{C187S}, *OsHIPP21*^{C133S}, *OsHIPP39*^{C190S},
549 *OsHIPP41*^{C152S}*)* in the pDONR constructs*,* and mutations in AVR-Pia to give *AVR-Pia-H3*,
550 were introduced by site-directed mutagenesis PCR using Phusion High-Fidelity DNA
551 Polymerase (Thermo Fisher Scientific) and mutation-specific primers listed in **Supplementary**
552 **Table S6**.

553 Gateway® LR recombination using LR Clonase® II mix (Thermo Fisher Scientific) was used
554 to transfer *OsH(I)PPs* and $RGA5_{Cter}$[11] (883-1116 aa) into Gateway®-compatible destination
555 vectors, including a modified Y2H vector pGBKT7-GW[70] and the plant expression vector pBIN-
556 35S-3Flag-Cluc-GWY (Deslandes et al., unpublished). Similarly, MAX effector
557 pDONR constructs were recombined into a modified pGADT7-GW[70] and pBIN-35S-3HA-Nluc-
558 GWY (Deslandes et al., unpublished) destination vectors. The pBIN-35S-3HA-Nluc-GWY and
559 pBIN-35S-3Flag-Cluc-GWY vectors were generated by ligation of a 3HA-Nluc-FrameB or
560 3Flag-Cluc-FrameB fragment, respectively, into a XhoI/XbaI digested pBIN-35S vector.

561 Previously published expression constructs for AVR1-CO39, AVR-Pia, and AVR-Pia-H3[4,12,13]
562 were used for protein production in the present study.

563 A complete list of plasmids used in this study is provided in **Supplementary Table S7.**

564 **Yeast two-hybrid**

565 The yeast strain Y2HGold (mating type a; Takara Bio) was transformed with the bait construct
566 expressed from the pGBKT7 vector, which contains the GAL4-BD and the *TRP1* marker gene.
567 These constructs included previously described HMA domains [49], as well as newly generated
568 constructs: OsHIPP21-HMA, $OsH(I)PP^{WT}$ FL and $OsH(I)PP^{C/S}$ FL. The yeast strain Y187
569 (mating type α; Takara Bio) was transformed with the prey construct (MAX effectors)
570 expressed from the pGADT7 vector, which carries the GAL4-AD and the *LEU2* marker
571 gene. Yeast transformation was performed using a lithium acetate (LiAc)-based protocol
572 according to the Yeastmaker Yeast Transformation System (Takara Bio). Transformed yeast
573 cells were plated on synthetic defined (SD) media lacking either tryptophan (-W) or leucine (-
574 L) and incubated at 30 °C for 3 days.

575 Mating of the transformed yeast strains followed the Matchmaker Gold Yeast Two-Hybrid
576 System User Manual (Takara Bio). Diploid yeast cells were selected on SD/-L-W plates (SD
577 medium lacking leucine and tryptophan) after incubation at 30 °C for 2 days. For Y2H assays,
578 diploid yeast cells were inoculated in SD/-L-W medium, grown for 24 hours at 28°C with
579 shaking at 100 rpm, then pelleted and washed twice with sterile water. Serial 10-fold dilutions
580 (10^{-1}, 10^{-2}, and 10^{-3}) were spotted onto SD selection plates: SD/-L-W (growth control), SD/-
581 L-W-H (lacking leucine, tryptophan, and histidine), SD/-L-W-H supplemented with varying
582 concentrations of 3-amino-1,2,4-triazole (3AT). After 7 days incubation at 30 °C, plates were
583 photographed using the presentation station UF-130DX (Samsung).

584 **Yeast two-hybrid cDNA library screening**

585 The Y2H cDNA library derived from the rice cultivar CO39 and the BD:dSP-AVR-Pia construct,
586 have been previously described[11,47]. Library screening followed the Matchmaker Gold Y2H
587 system protocol (Takara Bio). Mating was performed between the Y2H Gold strain harbouring
588 GAL4-BD:AVR-Pia and the Y187 strain carrying the CO39 cDNA library. Diploid yeasts were
589 plated on SD/-L-W-H medium and supplemented with 20 mM 3AT. Colonies that grew were
590 re-streaked onto fresh SD/-L-W-H medium containing 20 mM 3AT to confirm interaction-
591 dependent growth. Yeast colony PCR was used to amplify cDNA inserts from positive clones,
592 and PCR products were sequenced. Sequences were aligned to the cDNAs of two publicly
593 available annotations of the *Oryza sativa* cv. Nipponbare reference genome (IRGSP-1.0[71] and
594 MSU7.0)[72] using BLAST to identify the corresponding genes. Only genes for which the cDNA
595 inserts (or fragments of cDNAs) were cloned in-frame with the GAL4-AD were retained as
596 candidate AVR-Pia targets.

597 **Agrobacterium-mediated transient expression in *N. benthamiana***

598 *Agrobacterium tumefaciens* strains AGL1 (carrying split-luciferase constructs) and GV3101-
599 pMP90 (carrying 35S::P19) were grown overnight at 28°C in 5 mL LB medium supplemented
600 with appropriate antibiotics. Overnight cultures were pelleted at 4,000 x *g* for 10 minutes, and
601 pellets resuspended in 2 mL infiltration buffer (10 mM $MgCl_2$, 10 mM MES pH 5.6, 150 µM
602 acetosyringone). Bacterial suspensions were incubated in the dark for 2 hours. The optical
603 density at 600 nm (OD_{600}) was adjusted to 0.05 for 35S::P19 and 0.1 for OsH(I)PPs and MAX
604 effectors, respectively. In all infiltration mixes, 35S::P19 was co-infiltrated to suppress gene
605 silencing. Agrobacterial suspensions were mixed and infiltrated into leaves of 5–6-week-old
606 *N. benthamiana* plants using a needleless syringe. Leaf discs were harvested 2 days post-
607 infiltration for luminescence measurements or protein extraction. *N. benthamiana* plants were
608 grown in a growth chamber on soil under a 16-hour light / 8-hour dark cycle, at 20 °C and 65
609 - 75% relative humidity.

610 **Split luciferase assay**

611 For luminescence measurements, 4 mm leaf discs (collected using a Miltex Biopsy Punch
612 (Delta Microscopie)) were placed into wells of a white 96-well plate containing water. The
613 water was removed and replaced with a 1 mM Xenolight D-luciferin-K^+ salt bioluminescent
614 substrate solution (Perkin Elmer). Luminescence was quantified using a Spark® microplate
615 reader (Tecan) over three cycles of 10 minutes each. For all experiments, data from the third
616 cycle were used for analysis. Each interaction was tested with eight technical replicates (eight
617 leaf discs per plate from four individual plants per biological replicate, unless otherwise
618 indicated in the figure legend). The luminescence assay was performed in three independent

619 experiments. Statistical analyses from three independent replicates (24 leaf discs in total,
620 unless otherwise indicated in the figure legend) and data visualisation were done using R
621 (version 4.4.1). Multiple comparisons were performed using pairwise Wilcoxon tests followed
622 by a Benjamini-Hochberg p-value adjustment with the stats package. Boxplots were generated
623 using the ggplot2 package.

624 **Protein extraction and Western blotting**

625 Protein extraction from yeast was performed using a post-alkaline extraction protocol, as
626 described by Kushnirov[73]. For BD-OsHIPP14/19/20/39/41 and AD-MAX, yeast crude extracts
627 were resuspended in 50 µL of 1x LDS loading buffer (1x Bolt™ LDS sample buffer (Thermo
628 Fisher Scientific), 1x NuPAGE™ sample reducing agent (Thermo Fisher Scientific)), boiled at
629 95°C for 10 minutes, and loaded onto a 10% NuPAGE™ Bis-Tris gels (Invitrogen). For BD-
630 OsHPP09/10/11 and OsHIPP21, yeast crude extracts were resuspended in 50 µL of 1x SDS-
631 Tricine buffer (1x SDS-Tricine buffer (Thermo Fisher Scientific), 1x NuPAGE™ sample
632 reducing agent (Thermo Fisher Scientific)) and boiled at 85 °C for 2 minutes before loading
633 onto a 10-20% Tricine gel (Novax). Proteins were transferred to iBlot® nitrocellulose
634 membrane (Invitrogen) using the iBlot 2 Gel Transfer Device (program: 20 V 1 min, 23 V 4
635 min, 25 V, 2 min, Thermo Fisher Scientific), and analysed by immunoblotting.

636 For protein extraction from *N. benthamiana*, four leaf discs (0.8 mm diameter) were collected,
637 immediately frozen in liquid nitrogen and ground using a tissue homogeniser (Qiagen). The
638 ground plant material was solubilised in 200 µL extraction buffer (20 mM Tris-Hcl pH 7.5, 150
639 mM NaCl, 1 mM EDTA pH 8.0, 1% Triton X-100, 0.1% SDS, 5 mM DTT, 1x Protease inhibitor
640 cocktail (Sigma-Aldrich), 1x EDTA-free cOmplete protease inhibitor (Roche)). Protein extracts
641 were centrifuged at 18,000 x *g* for 15 minutes at 4 °C, and the resulting supernatants retained.
642 2x LDS buffer (Bolt™ LDS sample buffer (Thermo Fisher Scientific) and NuPAGE™ sample
643 reducing agent (Thermo Fisher Scientific)) was added and samples were denatured at 70 °C
644 for 10 minutes. Proteins were resolved by electrophoresis on NuPAGE™ 4-12% Bis-Tris gels
645 (Invitrogen). Proteins were transferred to iBlot® nitrocellulose membrane (Invitrogen) as
646 described above and analysed by immunoblotting.

647 For immunodetection of proteins, rabbit anti-GAL4-BD (sc-577, Santa Cruz Biotechnology,
648 1:2,000), goat anti-rabbit IgG-HRP (1:20,000, Sigma-Aldrich, A0545), mouse anti-Flag M2-
649 HRP (1:60,000, Sigma-Aldrich) and rat anti-HA-HRP (clone 3F10, 1:1,1000, Roche) were
650 used. Chemiluminescence was detected using the Immobilon western kit (Millipore) or the
651 SuperSignal™ West Femto Maximum Sensitivity substrate (Thermo Fisher Scientific) and the
652 Syngene 680X EF GBOX imaging system (Syngene).

653 **Protein production and purification**

654 ***HMA domains***

655 HMA domains were produced with a cleavable N-terminal 6xHis-MBP tag from *E. coli* BL21
656 (DE3) or BL21 (DE3) pLysS. 700 mL cell cultures were grown in LB media at 37 °C from a
657 starting OD_{600} of 0.05-0.07 to an OD_{600} of 0.5-0.8. Protein production was induced by addition
658 of IPTG (final concentration 1 mM) and cultures were grown for a further 14-16 hours at 20
659 °C. Cells were pelleted by centrifugation and the pellets stored at -70 °C. Thawed pellets were
660 resuspended in 50 mM Tris-HCl pH 7, 300 mM NaCl, 30 mM imidazole supplemented with
661 cOmplete EDTA-free protease inhibitor cocktail (Roche). Cells were lysed by sonication and
662 the lysate clarified by centrifugation at 40,000 x *g* at 6 °C for 30 minutes. Subsequent
663 chromatography steps were carried out with an ÄKTA Pure system (Cytiva) at 4 °C. The
664 filtered (0.45 µm) supernatant was applied to a 5 ml HisTrap™ FF column (Cytiva) and, after
665 washing with 50 mM Tris-HCl pH 7, 300 mM NaCl, 30 mM imidazole, bound protein was step-
666 eluted with 50 mM Tris-HCl pH 7, 300 mM NaCl, 500 mM imidazole. The eluate was injected
667 onto a Superdex 75 26/60 size exclusion chromatography column (Cytiva) pre-equilibrated in
668 50 mM Tris-HCl pH 7, 150 mM NaCl. Fractions containing the fusion protein were incubated
669 with 3C protease overnight at 4 °C. HMA domains were separated from the 6xHis-MBP tag
670 and GST-tagged 3C protease by injecting the protease-treated sample onto a 5 ml HisTrap™
671 FF column (Cytiva), 5 ml MBPTrap™ HP column (Cytiva), and 5 ml GSTrap™ HP column
672 (Cytiva) connected in tandem and equilibrated in 50 mM Tris-HCl pH 7, 300 mM NaCl, 30 mM
673 imidazole. Pooled fractions containing HMA domains were concentrated to < 8 ml then
674 injected onto a Superdex 75 26/60 size exclusion chromatography column (Cytiva) pre-
675 equilibrated in 50 mM Tris-HCl pH 7, 150 mM NaCl. Pooled fractions containing the purified
676 HMA domains were concentrated. At each stage, fractions containing the HMA domain were
677 determined by SDS-PAGE. Samples were combined with 5X SDS loading buffer (60 mM Tris-
678 HCl pH 6.8, 25% glycerol, 4% SDS, 0.1% bromophenol blue, 10 mM DTT), heated at 95 °C
679 for 5 minutes, then loaded onto a Bolt™ 10 %, Bis-Tris gel (Invitrogen). After migration, gels
680 were stained in InstantBlue® Coomassie protein stain (Abcam). Final protein concentration
681 was determined using a Pierce™ BCA Protein Assay Kit (ThermoFisher Scientific), due to the
682 extreme molar extinction coefficients of the proteins (0 $M^{-1}cm^{-1}$ for OsHIPP21-HMA, 1490 M^{-}
683 $^{1}cm^{-1}$ for OsHPP-HMA domains) at 280 nm. Proteins were stored at -80 °C.

684 ***MAX effectors***

685 AVR-Pia, AVR-Pia-H3 and AVR1-CO39 were produced and purified as previously
686 described[4,12,13]. Concentrations of MAX effectors were determined from molar extinction
687 coefficients and absorbance at 280 nm.

688 **Analytical size exclusion chromatography**

689 Analytical size exclusion chromatography experiments were conducted using a Superdex 75
690 10/300 GL column (Cytiva) connected to an ÄKTA Pure system (Cytiva) at 4 °C. Running
691 buffer was 50 mM Tris pH 7, 150 mM NaCl, 1 mM DTT for experiments with AVR1-CO39 and
692 20 mM sodium citrate pH 5.6, 150 mM NaCl, 1 mM DTT for experiments with AVR-Pia and
693 AVR-Pia-H3. To investigate whether OsHPP09-HMA forms a complex with the effectors, the
694 two proteins were combined in a 1:1 molar ratio and incubated on ice for 1 h prior to analysis.
695 Each protein was also analysed alone, at a concentration equivalent to that present in the
696 mixture. For each experiment, 100 µl protein was injected onto the column and eluted at a
697 flow rate of 0.5 ml/min. 500 µl fractions were collected for analysis by SDS-PAGE (as
698 described in the protein purification section above).

699 **Circular dichroism spectroscopy**

700 Circular dichroism (CD) spectra were obtained using a Chirascan™ CD Spectrometer (Applied
701 Photophysics). Proteins were dialysed into 10 mM sodium phosphate, pH 7.2 using Slide-A-
702 Lyzer™ MINI dialysis devices (Thermo Fisher Scientific). 40 µl protein was used to fill a 0.1
703 mm cuvette. The sample compartment temperature was 20 °C. Spectra were obtained for
704 wavelengths from 180 nm to 260 nm with step size of 1 nm, bandwidth of 2 nm and time-per-
705 point of 2 s. Ten spectra were acquired for buffer and each sample. The average trace for
706 buffer was subtracted from the average trace for each protein. Units were converted from
707 millidegrees to mean residue molar ellipticity (MRME) using the Chirascan™ software.

708 **Nuclear magnetic resonance titration**

709 Samples of ^{15}N-labelled AVR-Pia (40 µM) alone and complexed to unlabelled OsHPP09-HMA
710 **(**1:0.5 or 1:1 molar ratio**)**, or OsHPP09-HMA mutants **(**1:1 molar ratio**)**, were prepared in 20
711 mM sodium citrate, pH 5.6, 150 mM NaCl, and 1mM DTT, with addition of 10% D_20 for the
712 lock and 1 µM DSS as internal reference for the ^{1}H dimension and indirectly referenced for
713 the ^{15}N dimension[74]. The backbone (Hn, Nh, Cα) and Cß resonances of ^{15}N,^{13}C-labeled AVR-
714 Pia complexed to OsHPP09-HMA (1:1 ratio) were assigned using three-dimensional (3D)
715 HNCO, HNCA, HN(CO)CACB, HN(CA)CO and HNCACB experiments recorded at 305K on a
716 Bruker Avance 800 MHz spectrometer equipped with a triple resonance (^{1}H, ^{15}N, ^{13}C) z-
717 gradient cryo-probe, as described in detail for AVR-Pia alone in solution[13]. Spectra were
718 processed using Topspin (v. 3.5pl6) and analysed with Cindy in-house software or CCPN[75]
719 [analysis v 2.5.2].

720 Chemical shift perturbations ($\Delta\delta$) were calculated using the equation[76]:

721 $$\Delta\delta = \sqrt{0.5\left[(\Delta\delta_H)^2 + \left(\frac{\Delta\delta_N}{5}\right)^2\right]}$$

722 $\Delta\delta_H$ and $\Delta\delta_N$ are the chemical shift differences measured in the proton dimension and nitrogen
723 dimension, respectively, of 2D [^{1}H,^{15}N] HSQC spectra recorded for AVR-Pia alone or in the
724 presence of OsHPP09-HMA (1:1 ratio). $\Delta\delta$ greater than $\overline{\Delta\boldsymbol{\delta}}$ + 1σ or $\overline{\Delta\boldsymbol{\delta}}$ + 2σ were considered
725 as significant or very significant, respectively, σ being the standard deviation measured on the
726 distribution of chemical-shift perturbations.

727 **Isothermal titration calorimetry (ITC)**

728 ITC experiments were performed using a MicroCal PEAQ-ITC (Malvern Panalytical). Proteins
729 were dialysed overnight into 20 mM sodium citrate pH 6.0, 150 mM NaCl, 1 mM TCEP.
730 Experiments were carried out at 25 °C with a reference power of 5 µcal/s. The calorimetric cell
731 was filled with purified HMA domain at 18 µM (OsHPP09-HMA), 35 µM (OsHIPP21-HMA and
732 OsHPP11-HMA) or 60 µM (OsHPP10-HMA). This was titrated with AVR-Pia at a concentration
733 10X greater than that of the HMA domain (180 uM, 350 uM or 600 uM). Each experiment
734 consisted of a single injection of 0.5 µL followed by 18 injections of 2 µL each at 150 s intervals
735 with a stirring speed of 750 rpm. Data were processed with the MicroCal PEAQ-ITC analysis
736 software (Malvern Panalytical). Experiments were carried out in triplicate.

737 **Crystallisation of OsHPP09-HMA and AVR-Pia**

738 Sitting drop, vapour diffusion crystallisation trials were set up in 96-well Swissci 3 lens
739 crystallisation plates using dragonfly and mosquito dispensing robots (SPT Labtech). 100 nL
740 of protein at 8.6 mg/ml was combined with 100 nL reservoir solution. Needle-like crystals were
741 observed in multiple conditions in the commercial Structure Screen 1 + 2 (HT-96; Molecular
742 Dimensions) and PEGs Suite (NeXtal) screens. Optimisation around these conditions yielded
743 crystals suitable for diffraction studies. The X-ray diffraction data used to solve the structure
744 were obtained from a crystal from 0.1 M MES pH 6.5, 0.2 M ammonium sulphate, 20% (w/v)
745 PEG 4000. The crystal was mounted in a nylon loop and flash-frozen in liquid nitrogen prior to
746 shipping to the European Synchrotron Radiation Facility (ESRF).

747 **X-ray diffraction data collection and processing, and model refinement**

748 X-ray diffraction data were collected on beamline MASSIF-1 (ID30A-1) at the ESRF. Data were
749 processed with the EDNA autoprocessing pipeline[77]. The scaled, unmerged data file was
750 passed to AIMLESS for data reduction[78,79] (implemented in CCP4i2[80]). The AVR-
751 Pia/OsHPP09-HMA structure was solved by molecular replacement with PHASER[81], using a

752 monomer of AVR-Pia (PDB accession 6Q76, chain B) and a monomer of OsHPP09-HMA
753 (modelled with ColabFold[82]). Iterative cycles of manual adjustment, refinement, and validation
754 were carried out using COOT[83], REFMAC5[84,85] and MolProbity[86,87]. Analysis of the interface
755 was performed with qtPISA[88]. Interatomic distances were measured and structure
756 superposition/RMSD calculations were performed with PyMOL v2.5.0 Open-Source[89].
757 Structure figures were prepared using the CCP4 molecular graphics (CCP4mg) software[90].

758 **Structural modelling of AVR-Pia/HMA complexes**

759 Structural modelling of AVR-Pia/HMA complexes was carried out with ColabFold v1.5.5 [82]
760 (based on AlphaFold2 Multimer v3[91,92]) and the AlphaFold3 web server (alphafoldserver.com;
761 models generated between 2024-05-27 and 2024-07-02)[93]. For models generated with
762 ColabFold, no template information from the PDB was used (template_mode: none) and
763 number of recycles was set to 20 (num_recycles: auto). Five models were generated for each
764 complex and relaxed using AMBER (num_relax: 5). Default settings were otherwise used. For
765 models generated with AlphaFold3, default settings were used. At the time of use, AlphaFold3
766 did not support excluding template information from the PDB. Five models were generated for
767 each complex using five different seed values. Interface analysis was carried out with
768 qtPISA[88].

Acknowledgements

We thank Mark Youles and Mark Banfield for generating and providing the pOPIN-GG vector and tag modules, Laurent Deslandes for providing the split-luciferase vectors, and Florian Veillet for providing the pFV79 construct. We thank Thorsten Langner for providing the Y2H HMA library. We thank Julie Noell for assistance with protein purification, Corinne Lionne and Manon Mallet for helpful discussions about ITC methods, and Christian Roumestand for advice about NMR data. We thank Sebastien Ribeiro, Laura Mathieu and Vincent Chochois for valuable discussions and support with data analysis. This work benefited from access to the NMR and RX facilities of the Integrated Biophysics and Structural Biology Platform (PIBBS) of the CBS. PIBBS is a GIS-IBISA platform and belongs to the French Infrastructure for Integrated Structural Biology (FRISBI), supported by the National Research Agency (ANR-10-INBS-05). We acknowledge the European Synchrotron Radiation Facility (ESRF) for provision of synchrotron radiation facilities. We thank the staff of the ESRF and EMBL Grenoble for assistance in using beamline ID30-A1 under proposal number mx-2409. This work was funded by the HORIZON EUROPE ERC-2019-STG-852482-ii-MAX awarded to Stella Cesari.

Author contributions

Josephine H.R. Maidment: Conceptualization; Data curation; Formal analysis; Investigation; Methodology; Project administration; Resources; Supervision; Validation; Visualization; Writing – original draft; Writing – review & editing. **Svenja C. Saile**: Conceptualization; Data curation; Formal analysis; Investigation; Methodology; Project administration; Resources; Supervision; Validation; Visualization; Writing – original draft; Writing – review & editing. **Aurélien Bocquet**: Investigation; Methodology; Resources; Validation; Writing – review & editing. **Céline Thivolle**: Investigation; Methodology; Resources; Validation; Writing – review & editing. **Léo Bourcet**: Investigation; Methodology; Resources; Validation; Writing – review & editing. **Lisa-Fatimatou Planel**: Investigation; Methodology; Resources; Validation; Writing – review & editing. **Muriel Gelin**: Methodology; Resources; Writing – review & editing. **Thomas Kroj**: Conceptualization; Writing – review & editing. **André Padilla**: Conceptualization; Methodology; Writing – review & editing. **Karine de Guillen**: Conceptualization; Data curation; Formal analysis; Investigation; Methodology; Project administration; Resources; Supervision; Validation; Visualization; Writing – original draft; Writing – review & editing. **Stella Cesari**: Conceptualization; Data curation; Formal analysis; Funding acquisition; Investigation; Methodology; Project administration; Resources; Supervision; Validation; Visualization; Writing – original draft; Writing – review & editing.

803 ## Competing interests

804 The authors declare that they have no conflicts of interest with the contents of this article.

805 ## Data availability

806 The protein structure of the complex between OsHPP09-HMA and AVR-Pia has been
807 deposited in the Protein Data Bank with accession number 9RSV (pdb_00009RSV). X-ray
808 diffraction data are publicly available via the European Synchrotron Radiation Facility [94].

809 # Figures

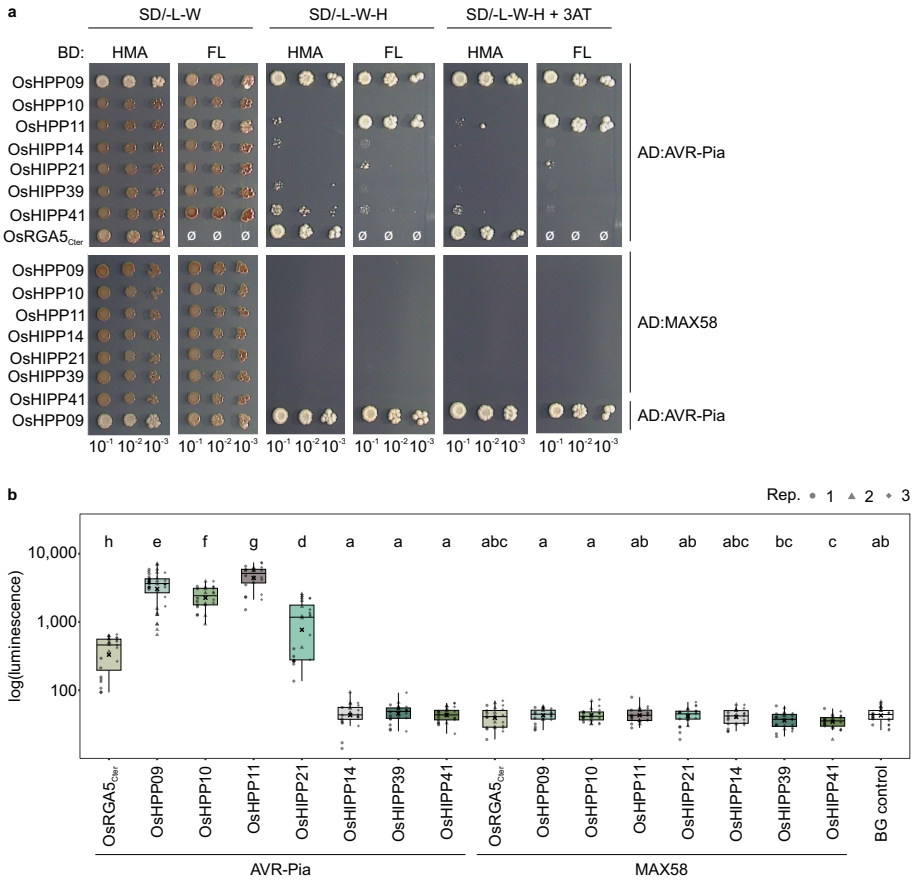

810

811 **Fig. 1. AVR-Pia interacts with OsH(I)PPs in yeast two-hybrid and in planta.**

812 **A** Y2H assay of AVR-Pia and MAX58 (both without signal peptides, ΔSP) with either the HMA
813 domain of OsH(I)PPs or full-length (FL) proteins. AVR-Pia/OsRGA5$_{Cter}$ (883-1116 aa) and
814 AVR-Pia/OsHPP09 served as positive controls (upper and lower panels, respectively). Serial
815 dilutions of diploid yeast clones were spotted onto synthetic defined (SD) media to monitor
816 growth (SD/-LW), or to assess protein-protein interactions (SD/-LWH and SD/-LWH
817 supplemented with 0.5 mM 3-amino-1,2,4-triazole (3AT)). Photos were taken after 7 days of
818 incubation. Ø indicates positions where no yeast was spotted. AD, GAL4 activation domain;
819 BD, GAL4 DNA binding domain. **b** Split luciferase complementation assay of AVR-Pia and
820 MAX58 (both ΔSP; fused to the N-terminal part of luciferase; 3xHA:NLuc:MAX) with FL
821 OsH(I)PPs (fused to the C-terminal part of luciferase: 3xFlag:CLuc:OsH(I)PP). Indicated
822 constructs were transiently co-expressed in *N. benthamiana* leaves and leaf discs were
823 harvested 2 days post-infiltration for luminescence measurements. AVR-Pia/OsRGA5$_{Cter}$
824 (883-1116 aa) was used as a positive control, and leaves infiltrated with P19 alone as
825 background (BG) control. Box plots show the median (line), mean (cross) and upper/lower
826 quartiles (box limits), whiskers extend to the most extreme data points within 1.5x the

827 interquartile range, with outliers plotted individually. Three independent replicates were
828 performed (n = 8 per replicate) except for AVR-Pia/OsHPP09: n = 16 in replicates 1 and 2.
829 Different letters indicate statistically significant differences based on a pairwise Wilcoxon test
830 (α = 0.05).

831

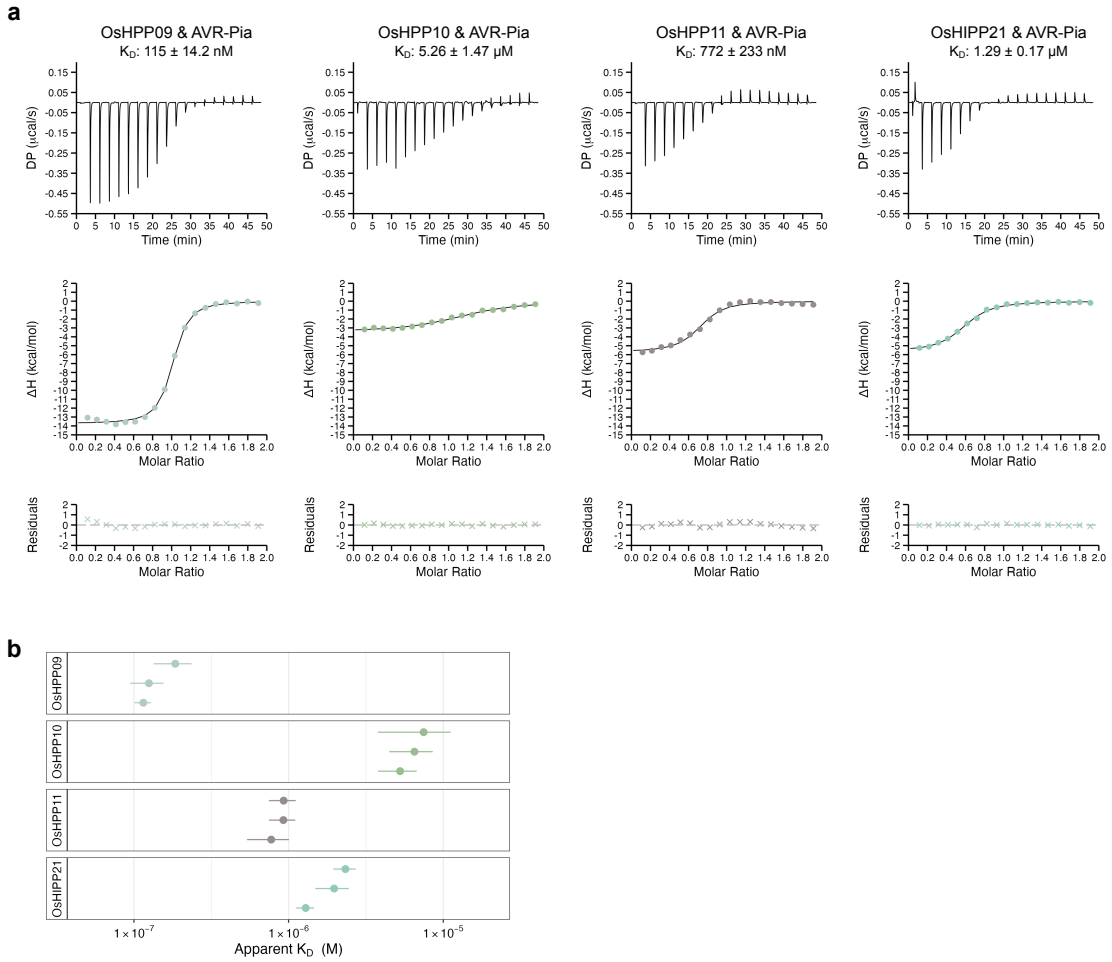

Fig. 2. AVR-Pia binds the HMA domains of OsH(I)PPs with varying affinities.

a Representative ITC experiments for each of the AVR-Pia/HMA interactions tested. Top panel shows the raw thermogram obtained from titration of AVR-Pia into a solution containing the purified HMA domains. Central panel shows the integrated heats (coloured dots) and binding isotherm fitted to a single site model (black line) using the MicroCal PEAQ-ITC analysis software (Malvern Panalytical). Bottom panel shows the differences (coloured crosses) between the modelled and observed values (residuals). **b** Dot plot representation of the apparent K_D for each of the AVR-Pia/HMA interactions in three independent experiments. Coloured dots represent the K_D values determined in each replicate with coloured lines representing the error associated with the K_D value as determined by the MicroCal PEAQ-ITC analysis software (Malvern Panalytical).

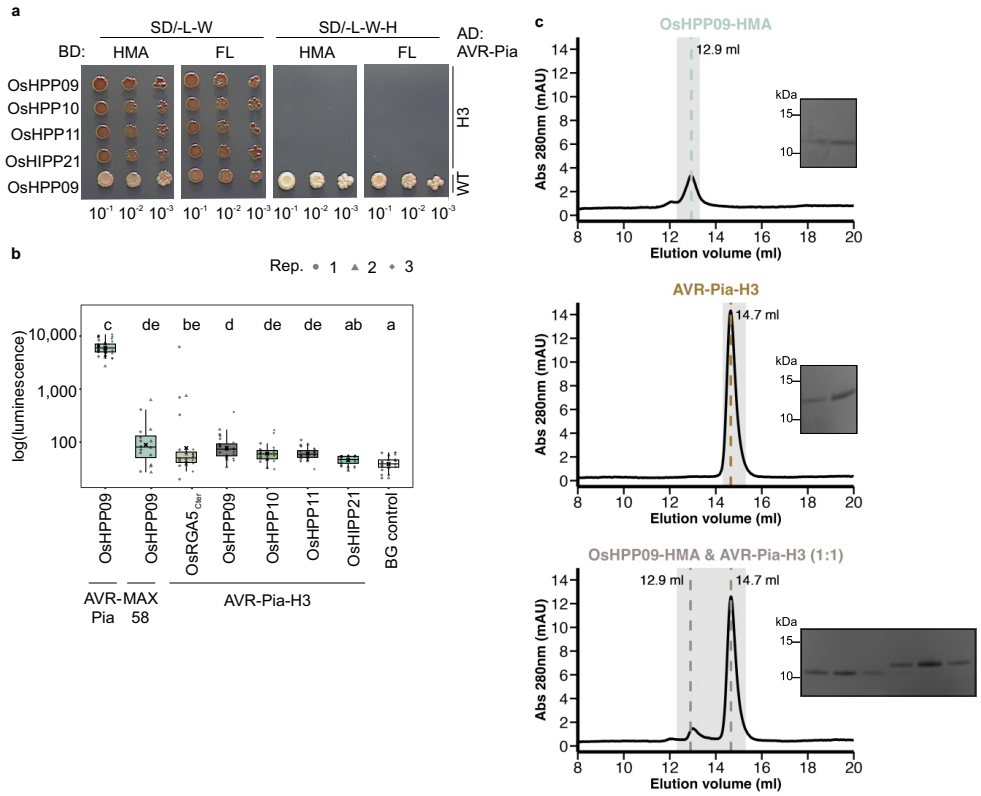

Fig. 3. AVR-Pia-H3 does not interact with OsHPP09, OsHPP10, OsHPP11 and HIPP21.

a Y2H interaction analysis between AVR-Pia-H3 (ΔSP) and either the HMA domain of OsH(I)PPs or full-length (FL) proteins. OsHPP09/AVR-Pia served as positive control. Serial dilutions of diploid yeast were spotted onto synthetic defined (SD) media to monitor growth (SD/-LW) or to assess protein-protein interactions (SD/-LWH). Photos were taken after 7 days of incubation. AD, GAL4 activation domain; BD, GAL4 DNA binding domain. **b** Split luciferase complementation assay of AVR-Pia-H3 (ΔSP; fused to the N-terminal part of luciferase; 3xHA:NLuc:MAX) with FL OsH(I)PPs (fused to the C-terminal part of luciferase: 3xFlag:CLuc:OsH(I)PP). Indicated constructs were transiently co-expressed in *N. benthamiana* leaves and leaf discs were harvested 2 days post-infiltration for luminescence measurements. AVR-Pia/OsHPP09 served as a positive control, MAX58/OsHPP09 and AVR-Pia-H3/OsRGA5$_{Cter}$ (883-1116 aa) as negative controls, and leaves infiltrated with P19 alone as background (BG) control. Box plots show the median (line), mean (cross) and upper/lower quartiles (box limits), whiskers extend to the most extreme data points within 1.5x the interquartile range, with outliers plotted individually. Three independent replicates were performed, with n = 8 per combination per replicate. Due to experimental constraints, for AVR-Pia/OsHPP09, n = 16 in replicates 1 and 2. Data points are shown with shapes indicating the replicate. Different letters indicate statistically significant differences based on a pairwise Wilcoxon test (α = 0.05). **c** Analytical gel filtration traces obtained from injection of OsHPP09-

865 HMA alone (top panel), AVR-Pia-H3 alone (middle panel) and the proteins combined (1:1
866 molar ratio; bottom panel). Significant peaks are indicated by coloured dashed lines with
867 elution volume labelled. SDS-PAGE gel inserts show fractions from peak elution volumes
868 indicated by grey shaded regions. OsHPP09-HMA absorbs light at 280 nm poorly (molar
869 extinction coefficient: 1490 $M^{-1}cm^{-1}$) so the peak corresponding to OsHPP09-HMA is small.

870

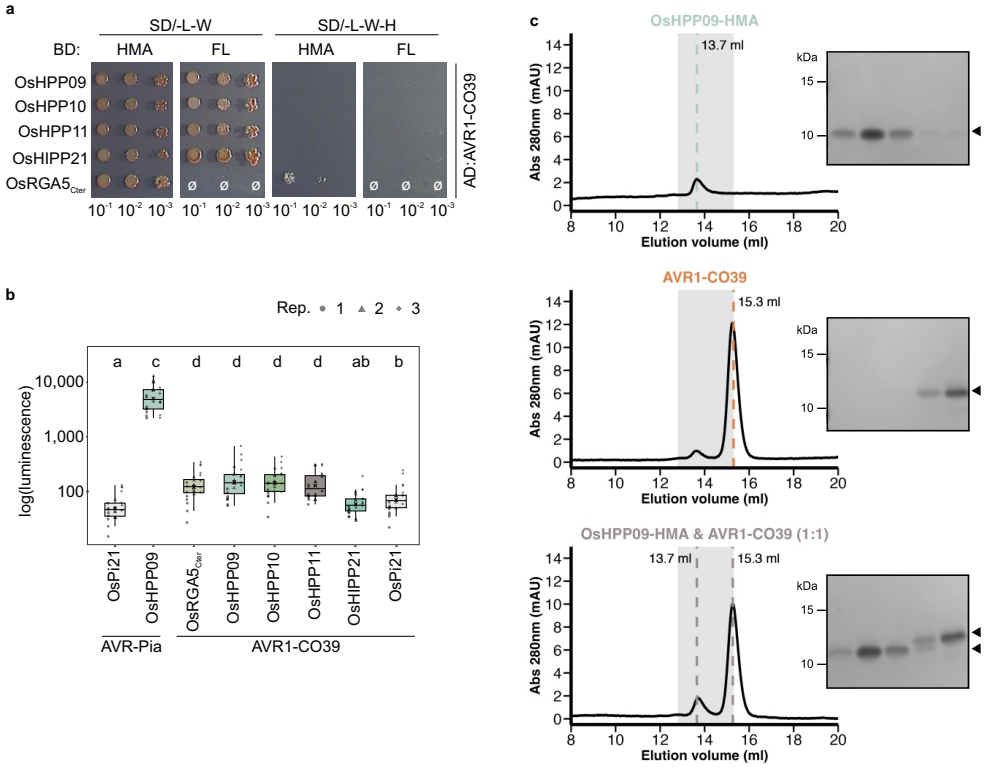

871

872 **Fig. 4. OsH(I)PPs interacting with AVR-Pia do not interact with AVR1-CO39.**

873 **a** Y2H interaction analysis between AVR1-CO39 (ΔSP) and either the HMA domain of
874 OsH(I)PPs or full-length (FL) proteins. AVR1-CO39/OsRGA5$_{Cter}$ (883-1116 aa) served as a
875 positive control. Serial dilutions of diploid yeast were spotted onto synthetic defined (SD)
876 media to monitor growth (SD/-LW) or to assess protein-protein interactions (SD/-LWH).
877 Photos were taken after 7 days of incubation. Ø indicates positions where no yeast was
878 spotted. AD, GAL4 activation domain; BD, GAL4 DNA binding domain. **b** Split-luciferase
879 complementation assay of ΔSP AVR1-CO39 with FL OsH(I)PPs and OsRGA5$_{Cter}$ (883-1116
880 aa). MAX effectors were fused to the N-terminal parts of luciferase (3xHA:NLuc:MAX), while
881 OsH(I)PP FL proteins and OsRGA5$_{Cter}$ were fused to its C-terminal part
882 (3xFlag:CLuc:OsH(I)PP/OsRGA5$_{Cter}$). Constructs were transiently co-expressed in *N.*
883 *benthamiana* leaves and leaf discs were harvested 2 days post-infiltration for luminescence
884 measurements. AVR-Pia or AVR1-CO39 with OsPi21 served as negative controls and AVR-
885 Pia/OsHPP09 as a positive control. Box plots show the median (line), mean (cross) and
886 upper/lower quartiles (box limits), whiskers extend to the most extreme data points within 1.5x
887 the interquartile range, with outliers plotted individually. Three independent replicates were
888 performed, with n = 8 per combination per replicate. All data points are shown with shapes
889 indicating the replicate. Different letters indicate statistically significant differences based on a
890 pairwise Wilcoxon test (α = 0.05). **c** Analytical gel filtration traces obtained from injection of

891 OsHPP09-HMA alone (top panel), AVR1-CO39 alone (middle panel) and the proteins
892 combined (1:1 molar ratio; bottom panel). Significant peaks are indicated by coloured dashed
893 lines with elution volume labelled. SDS-PAGE gel inserts show fractions from peak elution
894 volumes indicated by grey shaded regions. The small peak at ~13.7 ml for AVR1-CO39 is
895 likely due to dimerisation of the AVR1-CO39 protein; the quantity of the dimer is insufficient to
896 observe a band on the SDS-PAGE gel. OsHPP09-HMA absorbs light at 280 nm poorly (molar
897 extinction coefficient: 1490 $M^{-1}cm^{-1}$) so the peak corresponding to OsHPP09-HMA is small.
898

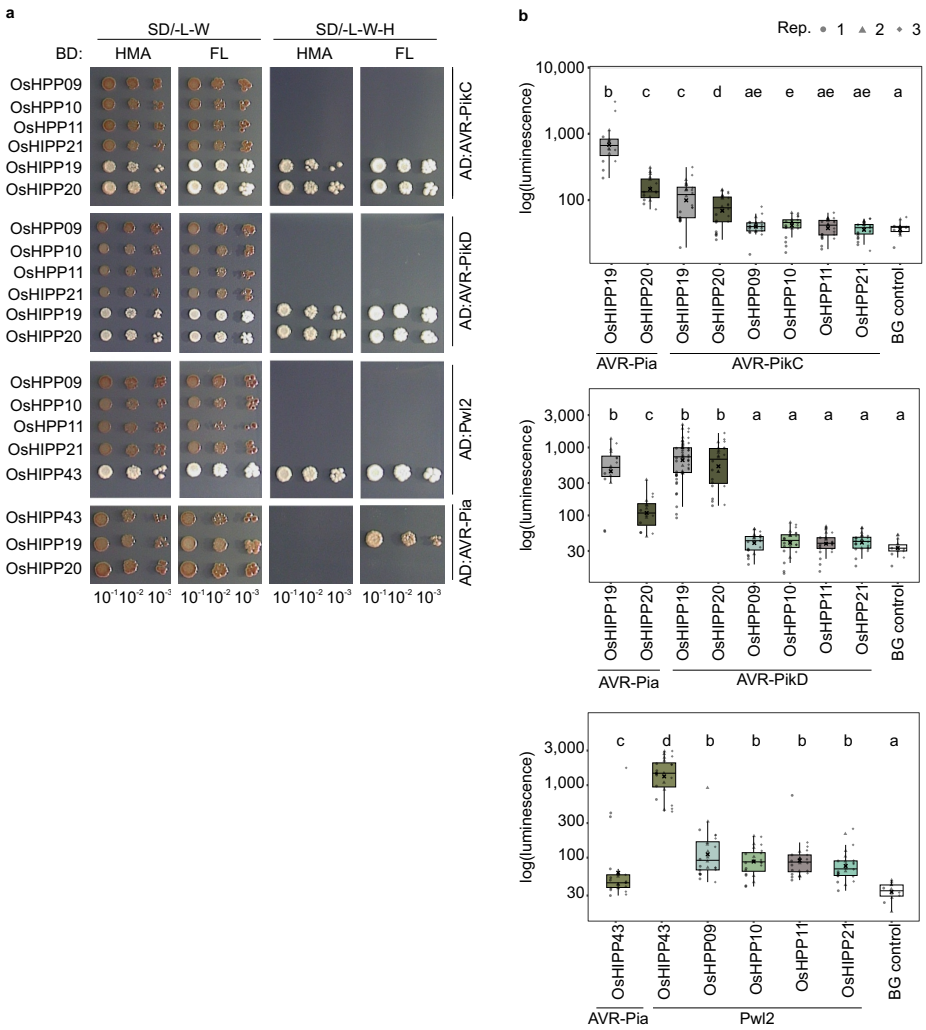

Fig. 5. OsH(I)PPs interacting with AVR-Pia do not interact with AVR-Pik or Pwl2.

a Y2H interaction analysis between AVR-PikC, AVR-PikD, Pwl2 and AVR-Pia (all ΔSP) and either the HMA domain of OsH(I)PPs or full-length (FL) proteins. OsHIPP19/AVR-PikC, OsHIPP20/AVR-PikC, OsHIPP19/AVR-PikD, OsHIPP20/AVR-PikD and OsHIPP43/Pwl2 served as positive controls. Serial dilutions of diploid yeast were spotted onto synthetic defined (SD) media to monitor growth (SD/-LW) or to assess protein-protein interactions (SD/-LWH). Photos were taken after 7 days of incubation. AD, activating domain; BD, binding domain. **b** Split luciferase complementation assay of MAX effectors (ΔSP; fused to the N-terminal part of luciferase: 3xHA:NLuc:MAX) with OsH(I)PP FL proteins (fused to the C-terminal part of luciferase: 3xFlag:CLuc:OsH(I)PP). AVR-PikC/AVR-PikD with OsHIPP19/20 and Pwl2 with OsHIPP43 served as positive controls, AVR-Pia with OsHIPP43 served as a negative control. Leaves infiltrated with P19 alone served as background (BG) control. Box plots show the median (line), mean (cross) and upper/lower quartiles (box limits), whiskers extend to the most extreme data points within 1.5x the interquartile range, with outliers plotted individually Three independent replicates were performed, with n = 8 per combination per replicate, except for

915 AVR-Pia/OsHIPP19 and AVR-Pia/OsHIPP20 in AVR-PikC and AVR-PikD panels: n = 4 in
916 replicates 1 and 3. For BG control in AVR-PikC and AVR-PikD panels: n = 3 in replicates 1
917 and 3 and for BG control in Pwl2 panel: n = 2 in replicates 1 and 3. For AVR-PikD/OsHIPP19
918 n = 16 in replicates 1 and 3 and n = 24 in replicate 2. Data points are shown with shapes
919 indicating the replicate. Different letters indicate statistically significant differences based on a
920 pairwise Wilcoxon test (α = 0.05).
921

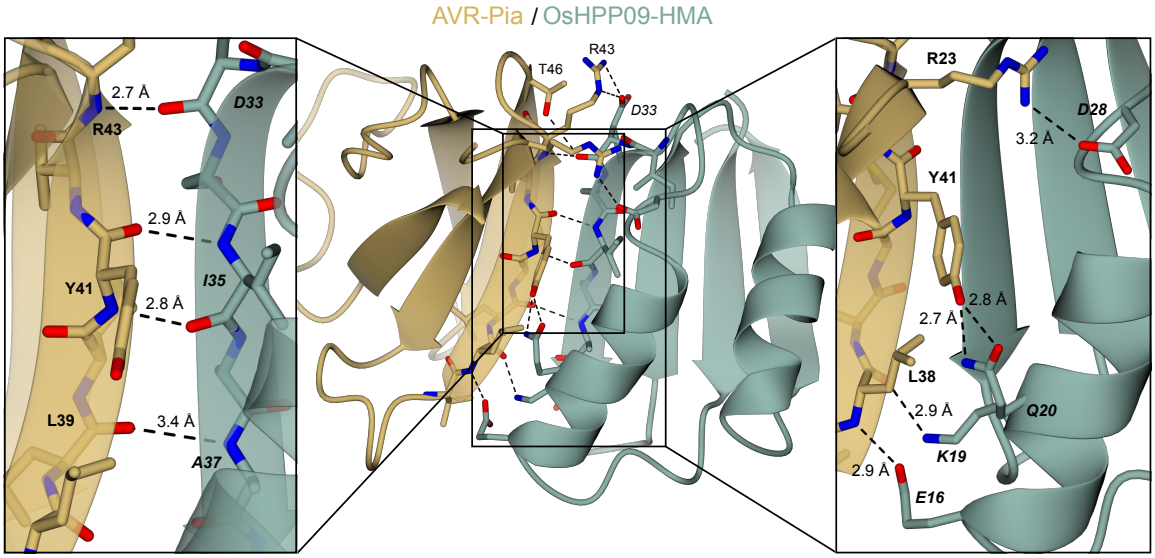

922

923 **Fig. 6. Crystal structure of the HMA domain of OsHPP09 in complex with AVR-Pia.**

924 The structures of OsHPP09-HMA and AVR-Pia are represented as teal and gold ribbons,
925 respectively. The amino acids comprising β2 of AVR-Pia and β2 of the HMA domain are
926 represented as cylinders. Side chains involved in intermolecular hydrogen bonds/salt bridges
927 are also represented as cylinders. Hydrogen bonds are represented by black dashed lines
928 labelled with the bond length. Left insert shows main chain hydrogen bonds between AVR-
929 Pia-β2 and OsHPP09-β2. Right insert shows intermolecular contacts between side chains of
930 residues in OsHPP09-α1 and AVR-Pia.

931

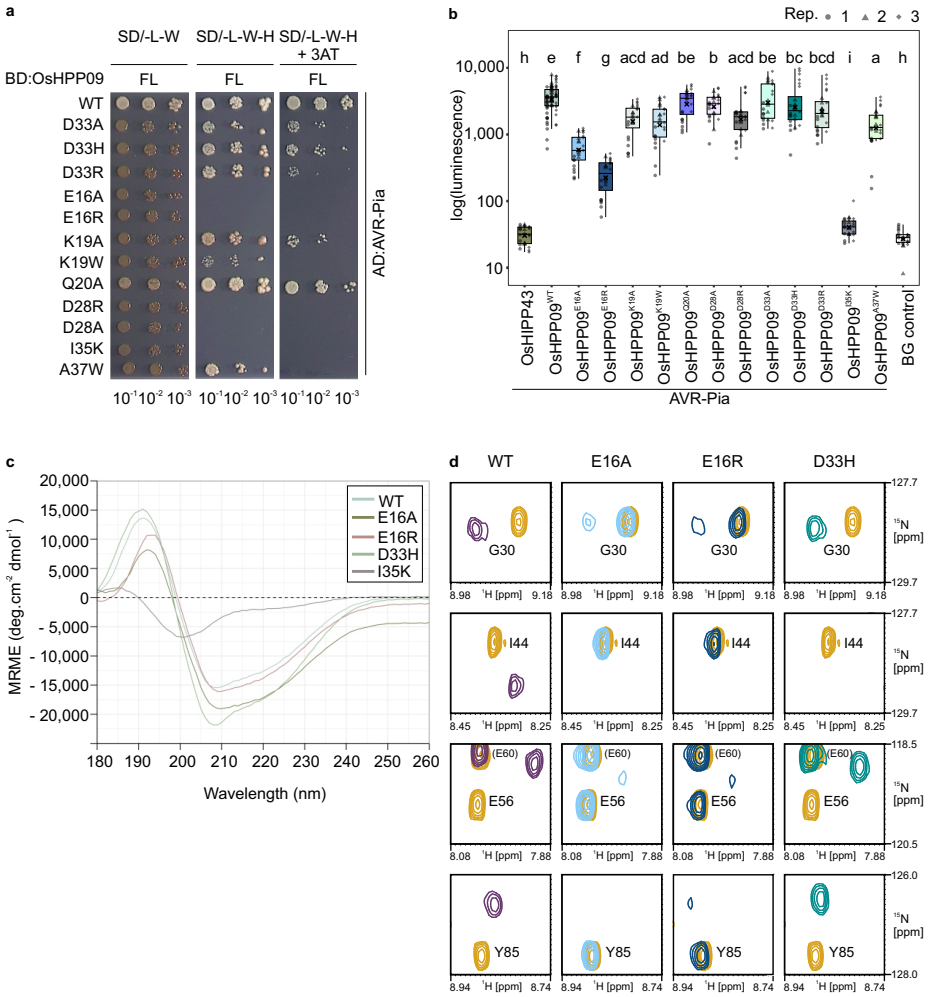

Fig. 7. Mutation of OsHPP09 E16 reduces AVR-Pia binding.

a Y2H interaction analysis between AVR-Pia (ΔSP) and full-length (FL) OsHPP09 carrying single point mutations. OsHPP09^{WT}/AVR-Pia served as positive control. Serial dilutions of diploid yeast were spotted onto synthetic defined (SD) media to monitor growth (SD/-LW) or to assess protein-protein interactions (SD/-LWH and SD/-LWH supplemented with 5 mM 3AT). Photos were taken after 7 days of incubation. AD, activating domain; BD, binding domain. **b** Split luciferase complementation assays of AVR-Pia (ΔSP; fused to the N-terminal part of luciferase; 3xHA:NLuc:AVR-Pia) with FL OsHPP09 carrying indicated mutations (fused to the C-terminal part of luciferase: 3xFlag:CLuc:OsHPP09). Co-expression of AVR-Pia with OsHPP09 served as a positive control, co-expression of OsHIPP43 with AVR-Pia as a negative control. Leaves infiltrated with P19 alone served as background (BG) control. Box plots show the median (line), mean (cross) and upper/lower quartiles (box limits), whiskers extend to the most extreme data points within 1.5x the interquartile rang, with outliers plotted individually. Three independent replicates were performed, with n = 8 per combination per replicate. Data points are shown with shapes corresponding to the replicate. Different letters

948 indicate statistically significant differences based on a pairwise Wilcoxon test (α = 0.05). **c**
949 Circular dichroism (CD) spectra obtained for WT OsHPP09-HMA (pale blue) and variants
950 carrying E16A, E16R, I35K or D33H mutations. Negative peaks at 222 nm/208 nm and a
951 positive peak at 193 nm indicate α-helices while a negative peak at 218 nm and positive peak
952 at 195 nm indicate β-sheets, consistent with the βαββαβ HMA domain topology. Low ellipticity
953 above 210 nm and a negative peak at 200 nm indicates disorder. **d** Overlays of cross-peaks
954 from HSQC spectra corresponding to residues G30, I44, E56 and Y85 of ^{15}N-labelled AVR-
955 Pia alone (orange) and in the presence of either WT OsHPP09-HMA or variants carrying
956 E16A, E16R or D33H mutations (blue/green/purple). Overlays of the full spectra are provided
957 in **Supplementary Figures 21-23**.

958

959 ## References

960 1. Baudin, M. *et al.* Pyricularia oryzae: Lab star and field scourge. *Mol Plant Pathol* **25**,
961 (2024).

962 2. Savary, S. *et al.* The global burden of pathogens and pests on major food crops. *Nat*
963 *Ecol Evol* **3**, 430–439 (2019).

964 3. Oliveira-Garcia, E., Yan, X., Oses-Ruiz, M., de Paula, S. & Talbot, N. J. Effector-
965 triggered susceptibility by the rice blast fungus Magnaporthe oryzae. *New Phytologist*
966 **241**, 1007–1020 (2024).

967 4. Le Naour--Vernet, M. *et al.* Structure-guided insights into the biology of fungal effectors.
968 *New Phytologist* **246**, 1460–1477 (2025).

969 5. de Guillen, K. *et al.* Structure analysis uncovers a highly diverse but structurally
970 conserved effector family in phytopathogenic fungi. *PLoS Pathog* **11**, (2015).

971 6. Lahfa, M. *et al.* Does a Similar 3D Structure Mean a Similar Folding Pathway? The
972 Presence of a C-Terminal α-Helical Extension in the 3D Structure of MAX60 Drastically
973 Changes the Folding Pathway Described for Other MAX-Effectors from Magnaporthe
974 oryzae. *Molecules* **28**, 6068 (2023).

975 7. Lahfa, M. *et al.* The structural landscape and diversity of Pyricularia oryzae MAX
976 effectors revisited. *PLoS Pathog* **20**, e1012176 (2024).

977 8. Le Naour--Vernet, M. *et al.* Adaptive evolution in virulence effectors of the rice blast
978 fungus Pyricularia oryzae. *PLoS Pathog* **19**, e1011294 (2023).

979 9. Maidment, J. H. R. *et al.* Multiple variants of the fungal effector AVR-Pik bind the HMA
980 domain of the rice protein OsHIPP19, providing a foundation to engineer plant defense.
981 *Journal of Biological Chemistry* **296**, (2021).

982 10. Zdrzałek, R. *et al.* Bioengineering a plant NLR immune receptor with a robust binding
983 interface toward a conserved fungal pathogen effector. *Proc Natl Acad Sci U S A* **121**,
984 e2402872121 (2024).

985 11. Liao, J. *et al.* Pathogen effectors and plant immunity determine specialization of the
986 blast fungus to rice subspecies. *Elife* **5**, (2016).

987 12. Cesari, S. *et al.* The rice resistance protein pair RGA4/RGA5 recognizes the
988 Magnaporthe oryzae effectors AVR-Pia and AVR1-CO39 by direct binding. *Plant Cell*
989 **25**, 1463–1481 (2013).

990 13. Guo, L. *et al.* Specific recognition of two MAX effectors by integrated HMA domains in
991 plant immune receptors involves distinct binding surfaces. *Proc Natl Acad Sci U S A*
992 **115**, 11637–11642 (2018).

993 14. Ortiz, D. *et al.* Recognition of the Magnaporthe oryzae effector AVR-Pia by the decoy
994 domain of the rice NLR immune receptor RGA5. *Plant Cell* **29**, 156–168 (2017).

995 15. Cesari, S. Multiple strategies for pathogen perception by plant immune receptors. *New*
996 *Phytologist* **219**, 17–24 (2018).

997 16. Cesari, S., Bernoux, M., Moncuquet, P., Kroj, T. & Dodds, P. N. A novel conserved
998 mechanism for plant NLR protein pairs: The 'integrated decoy' hypothesis. *Front Plant*
999 *Sci* **5**, (2014).

1000 17. Kroj, T., Chanclud, E., Michel-Romiti, C., Grand, X. & Morel, J. B. Integration of decoy
1001 domains derived from protein targets of pathogen effectors into plant immune receptors
1002 is widespread. *New Phytologist* **210**, 618–626 (2016).

1003 18. Sarris, P. F., Cevik, V., Dagdas, G., Jones, J. D. G. & Krasileva, K. V. Comparative
1004 analysis of plant immune receptor architectures uncovers host proteins likely targeted
1005 by pathogens. *BMC Biol* **14**, 1–19 (2016).

1006 19. Bailey, P. C. *et al.* Dominant integration locus drives continuous diversification of plant
1007 immune receptors with exogenous domain fusions. *Genome Biol* **19**, 1–18 (2018).

1008 20. Oikawa, K. *et al.* The blast pathogen effector AVR-Pik binds and stabilizes rice heavy
1009 metal-associated (HMA) proteins to co-opt their function in immunity. *PLoS Pathog* **20**,
1010 e1012647 (2024).

1011 21. De Abreu-Neto, J. B., Turchetto-Zolet, A. C., De Oliveira, L. F. V., Bodanese Zanettini,
1012 M. H. & Margis-Pinheiro, M. Heavy metal-associated isoprenylated plant protein (HIPP):
1013 characterization of a family of proteins exclusive to plants. *FEBS J* **280**, 1604–1616
1014 (2013).

1015 22. Tehseen, M., Cairns, N., Sherson, S. & Cobbett, C. S. Metallochaperone-like genes in
1016 Arabidopsis thaliana. *Metallomics* **2**, 556–564 (2010).

1017 23. Crowell, D. N. & Huizinga, D. H. Protein isoprenylation: the fat of the matter. *Trends*
1018 *Plant Sci* **14**, 163–170 (2009).

1019 24. Kay, B. K., Williamson, M. P. & Sudol, M. The importance of being proline: the
1020 interaction of proline-rich motifs in signaling proteins with their cognate domains. *The*
1021 *FASEB Journal* **14**, 231–241 (2000).

1022 25. Dykema, P. E. *et al.* A new class of proteins capable of binding transition metals. *Plant*
1023 *Mol Biol* **41**, 139–150 (1999).

1024 26. Suzuki, N., Yamaguchi, Y., Koizumi, N. & Sano, H. Functional characterization of a
1025 heavy metal binding protein CdI19 from Arabidopsis. *Plant Journal* **32**, 165–173 (2002).

1026 27. Khan, I. U. *et al.* Identification of novel rice (Oryza sativa) HPP and HIPP genes tolerant
1027 to heavy metal toxicity. *Ecotoxicol Environ Saf* **175**, 8–18 (2019).

1028 28. Li, J. *et al.* Heavy metal stress-associated proteins in rice and Arabidopsis: genome-
1029 wide identification, phylogenetics, duplication, and expression profiles analysis. *Front*
1030 *Genet* **11**, (2020).

1031 29. Barr, Z. K., Werner, T. & Tilsner, J. Heavy Metal-Associated Isoprenylated Plant
1032 Proteins (HIPPs) at plasmodesmata: Exploring the link between localization and
1033 function. *Plants* **12**, (2023).

1034 30. Barth, O., Vogt, S., Uhlemann, R., Zschiesche, W. & Humbeck, K. Stress induced and
1035 nuclear localized HIPP26 from Arabidopsis thaliana interacts via its heavy metal
1036 associated domain with the drought stress related zinc finger transcription factor
1037 ATHB29. *Plant Mol Biol* **69**, 213–226 (2009).

1038 31. Barth, O., Zschiesche, W., Siersleben, S. & Humbeck, K. Isolation of a novel barley
1039 cDNA encoding a nuclear protein involved in stress response and leaf senescence.
1040 *Physiol Plant* **121**, 282–293 (2004).

1041 32. Cowan, G. H. *et al.* Potato mop-top virus co-opts the stress sensor HIPP26 for long-
1042 distance movement. *Plant Physiol* **176**, 2052–2070 (2018).

1043 33. Radakovic, Z. S. *et al.* Arabidopsis HIPP27 is a host susceptibility gene for the beet
1044 cyst nematode Heterodera schachtii. *Mol Plant Pathol* **19**, 1917–1928 (2018).

1045 34. Fukuoka, S. *et al.* Loss of function of a proline-containing protein confers durable
1046 disease resistance in Rice. *Science (1979)* **325**, 998–1001 (2009).

1047 35. Were, V. M. *et al.* The Magnaporthe oryzae effector Pwl2 alters HIPP43 localization to
1048 suppress host immunity. *Plant Cell* (2025).

1049 36. Huang, Z. *et al.* Small secreted effector protein from Fusarium sacchari suppresses
1050 host immune response by inhibiting ScPi21-induced cell death. *Mol Plant Pathol* **25**,
1051 e13414 (2024).

1052 37. Song, H. *et al.* The Meloidogyne graminicola effector MgMO289 targets a novel copper
1053 metallochaperone to suppress immunity in rice. *J Exp Bot* **72**, 5638–5655 (2021).

1054 38. Huang, Q. *et al.* CRISPR/Cas9-mediated mutagenesis of the susceptibility gene
1055 OsHPP04 in rice confers enhanced resistance to rice root-knot nematode. *Front Plant*
1056 *Sci* **14**, (2023).

1057 39. Niu, X. *et al.* A small secreted protein, RsMf8HN, in Rhizoctonia solani triggers plant
1058 immune response, which interacts with rice OsHIPP28. *Microbiol Res* **266**, 127219
1059 (2023).

1060 40. Zhang, X. *et al.* Isolation and characterisation of cDNA encoding a wheat heavy metal-
1061 associated isoprenylated protein involved in stress responses. *Plant Biol* **17**, 1176–
1062 1186 (2015).

1063 41. Huang, G. *et al.* Genome-wide characterization of heavy metal-associated
1064 isoprenylated plant protein gene family from Citrus sinensis in response to
1065 huanglongbing. *Front Plant Sci* **15**, (2024).

1066 42. Imran, Q. M. *et al.* Nitric oxide responsive heavy metal-associated gene AtHMAD1
1067 contributes to development and disease resistance in Arabidopsis thaliana. *Front Plant*
1068 *Sci* **7**, 232346 (2016).

1069 43. Bentham, A. R. *et al.* A single amino acid polymorphism in a conserved effector of the
1070 multihost blast fungus pathogen expands host-target binding spectrum. *PLoS Pathog*
1071 **17**, e1009957- (2021).

1072 44. Ashikawa, I. *et al.* Two adjacent nucleotide-binding site-leucine-rich repeat class genes
1073 are required to confer Pikm-specific rice blast resistance. *Genetics* **180**, 2267–2276
1074 (2008).

1075 45. Zdrzałek, R., Kamoun, S., Terauchi, R., Saitoh, H. & Banfield, M. J. The rice NLR pair
1076 Pikp-1/Pikp-2 initiates cell death through receptor cooperation rather than negative
1077 regulation. *PLoS One* **15**, (2020).

1078 46. Cesari, S. *et al.* New recognition specificity in a plant immune receptor by molecular
1079 engineering of its integrated domain. *Nat Commun* **13**, (2022).

1080 47. Varden, F. A. *et al.* Cross-reactivity of a rice NLR immune receptor to distinct effectors
1081 from the rice blast pathogen Magnaporthe oryzae provides partial disease resistance.
1082 *J Biol Chem* **294**, 13006–13016 (2019).

1083 48. Langner, T., Kellner, R., Harant, A., Terauchi, R. & Kamoun, S. A clone resource of
1084 cereal heavy-metal associated (HMA) domains— putative targets of plant pathogen
1085 effector proteins. Preprint at https://doi.org/10.5281/zenodo.5148558 (2021).

1086 49. Maqbool, A. *et al.* Structural basis of pathogen recognition by an integrated HMA
1087 domain in a plant NLR immune receptor. *Elife* **4**, e08709 (2015).

1088 50. Gómez De La Cruz, D., Zdrzałek, R., Banfield, M. J., Talbot, N. J. & Moscou, M. J.
1089 Molecular mimicry of a pathogen virulence target by a plant immune receptor. *bioRxiv*
1090 Preprint at https://doi.org/10.1101/2024.07.26.605320 (2024).

1091 51. Homma, F., Huang, J. & van der Hoorn, R. A. L. AlphaFold-Multimer predicts cross-
1092 kingdom interactions at the plant-pathogen interface. *Nat Commun* **14**, 6040 (2023).

1093 52. Ose, T. *et al.* Solution structure of an avirulence protein, AVR-Pia, from Magnaporthe
1094 oryzae. *J Biomol NMR* **63**, 229–235 (2015).

1095 53. Schymkowitz, J. *et al.* The FoldX web server: an online force field. *Nucleic Acids Res*
1096 **33**, W382–W388 (2005).

1097 54. Park, C. H. *et al.* The Magnaporthe oryzae effector AvrPiz-t targets the RING E3
1098 ubiquitin ligase APIP6 to suppress pathogen-associated molecular pattern–triggered
1099 immunity in rice. *Plant Cell* **24**, 4748–4762 (2012).

1100 55. Park, C. H. *et al.* The E3 ligase APIP10 connects the effector AvrPiz-t to the NLR
1101 receptor Piz-t in rice. *PLoS Pathog* **12**, (2016).

1102 56. Couch, B. C. *et al.* Origins of host-specific populations of the blast pathogen
1103 Magnaporthe oryzae in crop domestication with subsequent expansion of pandemic
1104 clones on rice and weeds of rice. *Genetics* **170**, 613–630 (2005).

1105 57. Tosa, Y. *et al.* Evolution of an avirulence gene, AVR1-CO39, concomitant with the
1106 evolution and differentiation of Magnaporthe oryzae. *Molecular Plant-Microbe*
1107 *Interactions* **18**, 1148–1160 (2005).

1108 58. Hála, M., Žárský, V., Swiezewska, E. & Surmacz, L. Protein prenylation in plant stress
1109 responses. *Molecules* **24**, 3906 (2019).

1110 59. Nawaz, G. *et al.* Knockout of Pi21 by CRISPR/Cas9 and iTRAQ-based proteomic
1111 analysis of mutants revealed new insights into M. oryzae resistance in elite rice line.
1112 *Genes (Basel)* **11**, 1–24 (2020).

1113 60. Tao, H. *et al.* Engineering broad-spectrum disease-resistant rice by editing multiple
1114 susceptibility genes. *J Integr Plant Biol* **63**, 1639–1648 (2021).

1115 61. Zhou, Y. *et al.* Engineering of rice varieties with enhanced resistances to both blast and
1116 bacterial blight diseases via CRISPR/Cas9. *Plant Biotechnol J* **20**, 876–885 (2022).

1117 62. Hanika, K. *et al.* Impairment of tomato WAT1 enhances resistance to vascular wilt fungi
1118 despite severe growth defects. *Front Plant Sci* **12**, 721674 (2021).

1119 63. Kieu, N. P., Lenman, M., Wang, E. S., Petersen, B. L. & Andreasson, E. Mutations
1120 introduced in susceptibility genes through CRISPR/Cas9 genome editing confer
1121 increased late blight resistance in potatoes. *Sci Rep* **11**, 1–12 (2021).

1122 64. Wolter, M., Hollricher, K., Salamini, F. & Schulze-Lefert, P. The mlo resistance alleles
1123 to powdery mildew infection in barley trigger a developmentally controlled defence
1124 mimic phenotype. *MGG Molecular & General Genetics* **239**, 122–128 (1993).

1125 65. Kusch, S. *et al.* Arabidopsis mlo3 mutant plants exhibit spontaneous callose deposition
1126 and signs of early leaf senescence. *Plant Mol Biol* **101**, 21–40 (2019).

1127 66. Garcia-Ruiz, H., Szurek, B. & Van den Ackerveken, G. Stop helping pathogens:
1128 engineering plant susceptibility genes for durable resistance. *Curr Opin Biotechnol* **70**,
1129 187–195 (2021).

1130 67. Weber, E., Engler, C., Gruetzner, R., Werner, S. & Marillonnet, S. A modular cloning
1131 system for standardized assembly of multigene constructs. *PLoS One* **6**, e16765
1132 (2011).

1133 68. Engler, C., Kandzia, R. & Marillonnet, S. A one pot, one step, precision cloning method
1134 with high throughput capability. *PLoS One* **3**, (2008).

1135 69. Bentham, A. R. *et al.* pOPIN-GG: A resource for modular assembly in protein
1136 expression vectors. *bioRxiv* Preprint at https://doi.org/10.1101/2021.08.10.455798
1137 (2021).

1138 70. Bernoux, M. *et al.* Structural and functional analysis of a plant resistance protein TIR
1139 domain reveals interfaces for self-association, signaling, and autoregulation. *Cell Host*
1140 *Microbe* **9**, 200–211 (2011).

1141 71. Matsumoto, T. *et al.* The map-based sequence of the rice genome. *Nature* **436**, (2005).

1142 72. Kawahara, Y. *et al.* Improvement of the Oryza sativa nipponbare reference genome
1143 using next generation sequence and optical map data. *Rice* **6**, (2013).

1144 73. Kushnirov, V. V. Rapid and reliable protein extraction from yeast. *Yeast* **16**, 857–860
1145 (2000).

1146 74. Wishart, D. S. *et al.* 1H, 13C and 15N chemical shift referencing in biomolecular NMR.
1147 *J Biomol NMR* **6**, 135–140 (1995).

1148 75. Vranken, W. F. *et al.* The CCPN data model for NMR spectroscopy: Development of a
1149 software pipeline. *Proteins: Structure, Function and Genetics* **59**, 687–696 (2005).

1150 76. Grzesiek, S. *et al.* The solution structure of HIV-1 Nef reveals an unexpected fold and
1151 permits delineation of the binding surface for the SH3 domain of Hck tyrosine protein
1152 kinase. *Nat Struct Biol* **3**, 340–345 (1996).

1153 77. Incardona, M. F. *et al.* EDNA: A framework for plugin-based applications applied to X-
1154 ray experiment online data analysis. *J Synchrotron Radiat* **16**, 872–879 (2009).

1155 78. Evans, P. R. An introduction to data reduction: space-group determination, scaling and
1156 intensity statistics. *Acta Crystallogr D Biol Crystallogr* **67**, 282 (2011).

1157 79. Evans, P. R. & Murshudov, G. N. How good are my data and what is the resolution?
1158 *Acta Crystallogr D Biol Crystallogr* **69**, 1204–1214 (2013).

1159 80. Agirre, J. *et al.* The CCP4 suite: integrative software for macromolecular
1160 crystallography. *Acta Crystallogr D Struct Biol* **79**, 449–461 (2023).

1161 81. McCoy, A. J. *et al.* Phaser crystallographic software. *J Appl Crystallogr* **40**, 658–674
1162 (2007).

1163 82. Mirdita, M. *et al.* ColabFold: making protein folding accessible to all. *Nat Methods* **19**,
1164 679–682 (2022).

1165 83. Emsley, P., Lohkamp, B., Scott, W. G. & Cowtan, K. Features and development of Coot.
1166 *Acta Crystallogr D Biol Crystallogr* **66**, 486–501 (2010).

1167 84. Murshudov, G. N., Vagin, A. A. & Dodson, E. J. Refinement of macromolecular
1168 structures by the maximum-likelihood method. *Acta Crystallogr D Biol Crystallogr* **53**,
1169 240–255 (1997).

1170 85. Murshudov, G. N. *et al.* REFMAC5 for the refinement of macromolecular crystal
1171 structures. *Acta Crystallogr D Biol Crystallogr* **67**, 355–367 (2011).

1172 86. Davis, I. W., Murray, L. W., Richardson, J. S. & Richardson, D. C. MolProbity: Structure
1173 validation and all-atom contact analysis for nucleic acids and their complexes. *Nucleic*
1174 *Acids Res* **32**, (2004).

1175 87. Chen, V. B. *et al.* MolProbity: All-atom structure validation for macromolecular
1176 crystallography. *Acta Crystallogr D Biol Crystallogr* **66**, 12–21 (2010).

1177 88. Krissinel, E. & Henrick, K. Inference of macromolecular assemblies from crystalline
1178 state. *J Mol Biol* **372**, 774–797 (2007).

1179 89. Schrödinger LLC. *The PyMOL Molecular Graphics System, Version 2.5.0 Open-*
1180 *Source*. (2015).

1181 90. McNicholas, S., Potterton, E., Wilson, K. S. & Noble, M. E. M. Presenting your
1182 structures: the CCP4mg molecular-graphics software. *Acta Crystallogr D Biol*
1183 *Crystallogr* **67**, 386–394 (2011).

1184 91. Evans, R. *et al.* Protein complex prediction with AlphaFold-Multimer. *bioRxiv* Preprint
1185 at https://doi.org/10.1101/2021.10.04.463034 (2022).

1186 92. Jumper, J. *et al.* Highly accurate protein structure prediction with AlphaFold. *Nature*
1187 **596**, 583–589 (2021).

1188 93. Abramson, J. *et al.* Accurate structure prediction of biomolecular interactions with
1189 AlphaFold 3. *Nature* **630**, 493–500 (2024).

1190 94. Maidment, J. H. R., Bocquet, A., Gelin, M., De Guillen, K. & Cesari, S. BAG Montpellier
1191 [Dataset]. (2025) doi:10.15151/ESRF-DC-2199982133.

1192